

This work was written as part of one of the author's official duties as an Employee of the United States Government and is therefore a work of the United States Government. In accordance with 17 U.S.C. 105, no copyright protection is available for such works under U.S. Law. Access to this work was provided by the University of Maryland, Baltimore County (UMBC) ScholarWorks@UMBC digital repository on the Maryland Shared Open Access (MD-SOAR) platform.

Please provide feedback

Please support the ScholarWorks@UMBC repository by emailing scholarworks-group@umbc.edu and telling us what having access to this work means to you and why it's important to you. Thank you.


Magnetic reconnection and kinetic waves generated in the Earth's quasi-parallel bow shock

Cite as: Phys. Plasmas **27**, 092901 (2020); <https://doi.org/10.1063/5.0012443>

Submitted: 30 April 2020 . Accepted: 18 August 2020 . Published Online: 18 September 2020

 N. Bessho,  L.-J. Chen,  S. Wang,  M. Hesse,  L. B. Wilson, and  J. Ng

COLLECTIONS

 This paper was selected as Featured



View Online



Export Citation



CrossMark

ARTICLES YOU MAY BE INTERESTED IN

[Prospectus on electron acceleration via magnetic reconnection](#)

Phys. Plasmas **27**, 100601 (2020); <https://doi.org/10.1063/5.0019338>

[Hybrid-Vlasov modeling of three-dimensional dayside magnetopause reconnection](#)

Phys. Plasmas **27**, 092903 (2020); <https://doi.org/10.1063/5.0020685>

[Electron Landau damping of kinetic Alfvén waves in simulated magnetosheath turbulence](#)

Phys. Plasmas **27**, 102901 (2020); <https://doi.org/10.1063/5.0021727>



Physics of Plasmas
Features in Plasma Physics Webinars

Register Today!

Magnetic reconnection and kinetic waves generated in the Earth's quasi-parallel bow shock

Cite as: Phys. Plasmas **27**, 092901 (2020); doi: [10.1063/5.0012443](https://doi.org/10.1063/5.0012443)

Submitted: 30 April 2020 · Accepted: 18 August 2020 ·

Published Online: 18 September 2020



View Online



Export Citation



CrossMark

N. Bessho,^{1,2,a)}  L.-J. Chen,²  S. Wang,^{1,2}  M. Hesse,^{3,4}  L. B. Wilson III,²  and J. Ng^{1,2} 

AFFILIATIONS

¹Department of Astronomy, University of Maryland, College Park, Maryland 20742, USA

²Heliophysics Science Division, NASA Goddard Space Flight Center, Greenbelt, Maryland 20771, USA

³Space Plasma Physics Group, University of Bergen, Bergen, Norway

⁴Southwest Research Institute, San Antonio, Texas 78228, USA

^{a)} Author to whom correspondence should be addressed: naoki.bessho@nasa.gov

ABSTRACT

Magnetic reconnection in quasi-parallel shocks, relevant to the Earth's bow shock, is studied by means of two-dimensional full particle-in-cell simulations. As the Alfvénic Mach number increases, the propagation direction of the waves excited in the transition region changes, and the shock becomes more turbulent with more reconnection sites. In the higher Mach number shock, abundant electron-only reconnection sites are generated with scales on the order of the ion skin depth or less. Non-reconnecting current sheets can also generate electron jets and energy dissipation can occur there as well. However, non-reconnecting current sheets with the magnetic field reversal typically show a smaller energy dissipation rate than reconnecting current sheets. In the shock transition region, two types of waves are responsible for driving reconnection: one has a wavelength around three ion skin depths (d_i), and the other has a wavelength less than $1 d_i$. Electron and ion distribution functions show that in regions where the former type of waves is excited, there are two ion beams and a single-peaked electron distribution. In contrast, in regions where the latter type of waves is excited, there are multiple electron and ion beams. The waves propagating obliquely to the magnetic field bend the magnetic field lines, and magnetic reconnection occurs where oppositely directed field lines come into contact.

Published under license by AIP Publishing. <https://doi.org/10.1063/5.0012443>

I. INTRODUCTION

Recent *in situ* observations of the Earth's bow shock have revealed a number of active magnetic reconnection sites, for instance, studies using Cluster observed many current sheets in the Earth's magnetosheath with magnetic reconnection signatures.^{1–3} NASA's Magnetospheric Multiscale (MMS) has also been observing the Earth's bow shock, and has identified a number of magnetic reconnection sites in the magnetosheath^{4–8} and in the shock transition region.^{9–12} Recently it was discovered, in the magnetosheath⁷ and the shock transition region,^{9,10,12} that reconnection can occur due to only electrons' kinetic effects, resulting in the formation of electron reconnection jets, and ions do not participate in the reconnection.⁷ This electron-only reconnection results from shock turbulence having electron-scale magnetic field structures, and ions cannot respond to such small-scale field gradients.

Shock driven turbulence is a key to understand magnetic reconnection in shocks. It has been demonstrated that quasi-parallel shocks (the shock normal angle $0^\circ < \theta < 45^\circ$) are more turbulent than

quasi-perpendicular shocks ($45^\circ < \theta < 90^\circ$) (for example, see a simulation result of Ref. 13). Space observations in the Earth's magnetosheath behind the quasi-parallel bow shock show more turbulent current sheets than behind the quasi-perpendicular shock.^{1,2} A recent statistical study based on MMS measurements in the transition region of the Earth's bow shock also shows the same tendency, and further indicates that reconnection is observed more often in high Mach number, quasi-parallel conditions.¹² In this study, we investigate the kinetic physics of waves excited in the shock transition region of quasi-parallel shocks to understand magnetic reconnection driven by shock turbulence, by means of two-dimensional full particle-in-cell (PIC) simulations.

Shock driven reconnection has been addressed in studies using kinetic numerical simulations, both hybrid PIC simulations^{13,14} and full PIC simulations.^{15–17} Studies of high Alfvénic Mach number ($M_A \sim 30\text{--}40$) perpendicular shocks,^{15,16} with parameters relevant to astrophysical shocks, show that the Weibel instability generates magnetic field fluctuations perpendicular to the initial magnetic field. The

result is the generation of turbulence and multiple magnetic reconnection sites. In contrast, studies of much weaker quasi-parallel shocks ($M_A \sim 10$), with parameters relevant to the Earth's bow shock,^{14,17} show that waves different from the Weibel instability are excited. These are responsible for generating reconnecting current sheets. The generation of reconnecting current sheets is correlated with the shock reformation. Our previous study, using a full PIC simulation,¹⁷ demonstrated that sub-ion scale magnetic islands generated in the shock turbulence are the sites of electron-only reconnection. In this study, we discuss kinetic waves responsible for creating current sheets, and the field structures, the reconnection rates, and the energy dissipation rates in reconnecting current sheets, as well as those of non-reconnecting current sheets.

It is currently not known which waves are responsible for generating reconnection sites in the Earth's bow shock. For quasi-parallel shocks, waves and instabilities have been studied by means of theory and numerical simulations. Dispersion analyses of ion-ion beam instabilities predict that ultra-low frequency (ULF) waves are excited by the interaction between the incident ion component and the reflected ion component.^{18,19} One-dimensional and two-dimensional hybrid and full PIC simulations also demonstrated ULF waves whose wavelengths are 10 to several tens of ion skin depths.^{20–28} Space measurements (Ref. 29 and references therein) as well as laboratory experiments³⁰ have been observing these predicted waves. Also, in a steepened wave structure such as SLAMS (short, large-amplitude magnetic structures),³¹ high-frequency waves such as whistler waves can be generated^{27,32} (for space observations, see Ref. 29 and references therein). It is important to elucidate what types of waves are responsible to generate reconnecting current sheets. In this study, we investigate two types of waves: one wave has a wavelength around a few ion skin depths, and the other wave has a wavelength less than one ion skin depth. We examine electron and ion distribution functions in regions of those two types of waves, which generate winding magnetic field lines and cause magnetic reconnection in shocks.

In Sec. II, we describe the simulation method in this study. In Sec. III A, we discuss shock propagation and magnetic reconnection, and we discuss reconnecting and non-reconnecting current sheets. In Sec. III B, we discuss two types of waves excited in the shock transition region, and electron and ion distribution functions that are responsible for instabilities. In Sec. IV, we give discussions and conclusions of this study.

II. SIMULATION METHOD

We use 2D PIC simulations to study magnetic reconnection in the transition and downstream regions in the Earth's quasi-parallel bow shock. In the simulation in the x - y coordinates, x is the direction of the shock normal. In the simulation domain, there are initially a uniform magnetic field $\mathbf{B}_0 = (B_{x0}, B_{y0}, 0)$ and an electric field $\mathbf{E}_0 = (0, 0, E_{z0})$. Therefore, y is parallel to the shock plane, and the x - y plane contains the magnetic field \mathbf{B}_0 . In the z direction, it is assumed that $\partial/\partial z = 0$. The ion and electron densities n_i and n_e , respectively, are also uniform with $n_i = n_e = n_0$ initially, at $t = 0$. The system size is $L_x \times L_y = 375d_i \times 51.2d_i = 15000 \times 2048$ grids, where d_i is the ion skin depth ($d_i = c/(4\pi n_0 e^2/m_i)^{1/2}$, c is the speed of light, e is the elementary charge, and m_i is the ion mass). Initially, 100 particles/cell are loaded for each species.

The y boundary is periodic, and both x boundaries are rigid walls at which particles are specularly reflected. At the two x boundaries, the electric fields are set to be $E_y = 0$ and $E_z = E_{z0}$ as a boundary condition. Particles move in accordance with the $\mathbf{E} \times \mathbf{B}$ drift speed perpendicular to the magnetic field, with an initially imposed bulk parallel velocity $V_{\parallel} = -cE_{z0}B_{x0}/(B_0B_{y0})$ for both ions and electrons (where $B_0 = (B_{x0}^2 + B_{y0}^2)^{1/2}$), so that the y component of the bulk drift velocity becomes zero, and the bulk drift velocity becomes $\mathbf{V}_d = (V_{xd}, 0, 0)$ (where $V_{xd} = -cE_{z0}/B_{y0}$ for both ions and electrons). Thus, all the particles initially move in the negative x direction. At $t = 0$, the velocity distribution functions are drifting Maxwellians with uniform ion and electron temperatures, T_i and T_e . At the boundary at $x = L_x$, we constantly inject particles whose temperature and drift speed are the same as the initial particles.

Near the maximum x boundary, $215d_i < x < 375d_i$, a wave damping region is placed to inhibit artificial wave growth due to particle injection at the boundary $x = 375d_i$.³³

The simulation parameters are the same as Ref. 17, which are as follows: a mass ratio of $m_i/m_e = 200$, where m_e is the electron mass, and the initial beta values $\beta_i = \beta_e = 1.0$, where $\beta_j = n_0 T_j / (B_0^2 / 8\pi)$ ($j = i$ or e). The ratio of the electron plasma-to-cyclotron frequency is $\omega_{pe}/\Omega_e = 4$, where $\omega_{pe} = (4\pi n_0 e^2 / m_e)^{1/2}$, $\Omega_e = eB_0 / m_e c$.

The shock normal angle θ —the angle between the shock normal (positive x direction) and the magnetic field \mathbf{B}_0 —is set to be 25° ; i.e., $\theta = \tan^{-1}(B_{y0}/B_{x0}) = 25^\circ$. We performed two runs, denoted Run 1 and Run 2. Run 1 uses $V_{xd} = -9v_A$, where v_A is the Alfvén speed based on B_0 and n_0 , and Run 2 uses $V_{xd} = -5v_A$. In both Run 1 and Run 2, the shock speed v_{sh} (which will be discussed below) is $11.4v_A$ and $6.5v_A$, respectively, both of which are smaller than the electron thermal speed, $v_{Te} = 14.4v_A$. This condition, $v_{sh} < v_{Te}$, is relevant to the Earth's bow shock. Further, under this condition, the plasma is stable to Buneman instability.

III. 2D PIC SIMULATIONS OF SHOCK-DRIVEN RECONNECTION

A. Structures of reconnecting/non-reconnecting current sheets

1. Shock propagation, reformation, and reconnection

In Fig. 1, panels (a)–(e) show a time sequence of the profile of B_y along $y = 25.6d_i$ in Run 1 ($V_{dx} = -9v_A$), at five different times, $\Omega_i t = 12.5, 14.06, 15.63, 17.19$, and 18.75 , where Ω_i is the ion cyclotron frequency based on B_0 . Each black dashed line represents the position of the shock front, where B_y becomes the maximum, which is 5–8 times B_0 . At $\Omega_i t = 15.63$, the shock reformation starts and the B_y in the foreshock region (around $x = 50d_i$) starts to grow.¹⁷ At $\Omega_i t = 18.75$, there is a new shock front around $x = 50d_i$, which is indicated by the blue dashed line, and the magnitude of B_y at the new shock front becomes comparable to that at the old shock front (red dashed line) around $x = 30d_i$. Based on the distance between the shock front at $\Omega_i t = 3.125$ (not shown), at $x = 10.5d_i$, and the new shock front at $\Omega_i t = 18.75$, at $x = 48.6d_i$, the shock speed is $v_{sh} = 11.4v_A$ (the Alfvén Mach number $M_A = 11.4$), considering the upstream drift speed of the bulk plasma in the simulation frame, $V_{dx} = -9v_A$.

Panels (f)–(j) display the result of Run 2 ($V_{dx} = -5v_A$). During the interval between $\Omega_i t = 12.50$ and 15.63 , the shock front (black

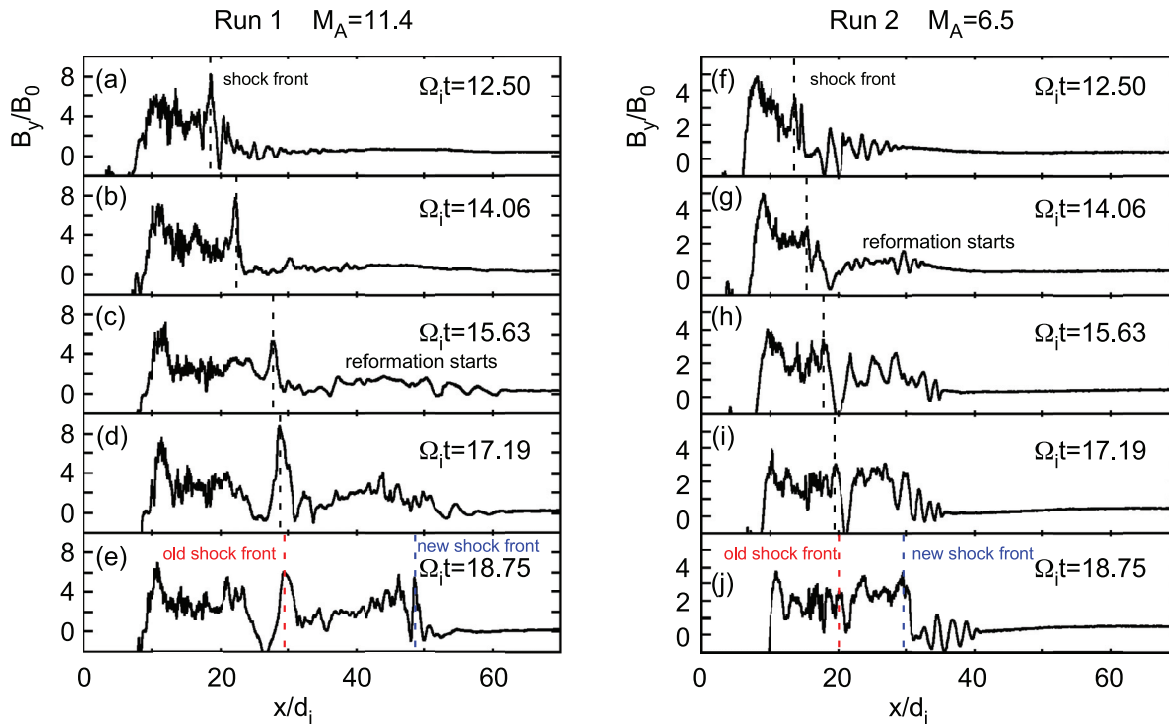


FIG. 1. 1D profiles of the magnetic field B_y at $y = 25.6d_i$ for Run 1 (a)–(e) and Run 2 (f)–(j). The black dashed line represents the shock front at each time. The red dashed line and the blue dashed line in the bottom panel at $\Omega_i t = 18.75$ are the old shock front and the new shock front generated by the shock reformation, respectively.

dashed line) is around $x = 15d_i$ to $18d_i$, where the maximum of $B_y \sim 3B_0$. The foreshock region around $x \sim 30d_i$ gradually grows, and the shock reformation proceeds between $\Omega_i t = 14.06$ and 17.19 . The magnetic field B_y in the new shock front becomes comparable to that at the old shock front, $\sim 3B_0$. Based on the shock front at $\Omega_i t = 3.125$ (not shown), at $x = 5.9d_i$, and the new shock front at $\Omega_i t = 18.75$, at $x = 29.5d_i$, the Alfvén Mach number is $M_A = 6.5$, considering the upstream fluid speed $V_d = -5v_A$, and M_A in Run 2 is almost twice smaller than M_A in Run 1.

Figure 2 shows the time evolution of the magnetic field lines (the contour of vector potential A_z) in Run 1 and Run 2, projected on the x - y plane. The left-hand column panels (a)–(e) are the plots for Run 1, and the right-hand column panels (f)–(j) are the plots for Run 2. Each panel (a)–(j) in Fig. 2 corresponds to the time in each (a)–(j) panel in Fig. 1, and the red dashed line (old shock front) and the blue dashed line (new shock front) in the bottom panel show the same positions of the old/new shock fronts in Fig. 1. In Run 1 (for $M_A = 11.4$), panels (a) and (b) show that the shock front (red dashed line) is around $x = 18d_i$ – $22d_i$, where the field lines become denser than the upstream region. In the shock transition region ($25d_i < x < 40d_i$), where the magnetic field strength is weaker than in the shock front and the downstream region, there are winding magnetic field lines. This undulation in the field lines is due to instabilities excited by interactions between reflected ions and incident ions, which will be discussed later. The wavelength of those winding field lines ranges from d_i to several d_i , and the size of the unstable region in the x direction becomes larger and larger as time progresses, comparing

panels (a) and (b). The shock plane (red dashed line) is not planar, but features wavy structures. Along the shock plane, the sign of B_x alternates, and there are compression and rarefaction of field lines, with a wavelength around $6d_i$ in the y direction.

As time elapses, the waves in the transition region grow and the winding magnetic field lines start to reconnect in some regions. At $\Omega_i t = 15.63$ [panel (c)], there are several magnetic islands in the transition region between $x = 27d_i$ and $40d_i$, as well as in the shock downstream between $x = 20d_i$ and the shock front at $x = 27d_i$. The shock reformation started before $\Omega_i t = 15.63$, and in panel (c), the B_y component of the magnetic field becomes larger in the region between $x = 40d_i$ and $50d_i$, compared with B_y in previous times [panels (a) and (b)]. During the interval between $\Omega_i t = 15.63$ and 18.75 [panels (c)–(e)], the shock reformation continues, and the steepening of B_y in the region between $x = 40d_i$ and $50d_i$ becomes much more significant. At $\Omega_i t = 17.19$ [panel (d)], there is a strong concentration of the magnetic field lines in front of the magnetic islands around $x = 40d_i$, and in front of those concentrated field lines, a strong instability that generates winding magnetic fields grows around $x = 50d_i$. At $\Omega_i t = 18.75$ [panel (e)], the new shock front forms, and the transition region around $x = 50d_i$ contains a number of small magnetic islands due to reconnection that occurs in the instability region. These are sites of electron-only reconnection,^{7,9,10} in which ions are just passing through the current sheet and only electrons participate in the reconnection. The detailed structure of one of those regions with electron-only reconnection has already been discussed in our previous paper.¹⁷ The region between the red dashed line (the old shock front) and the

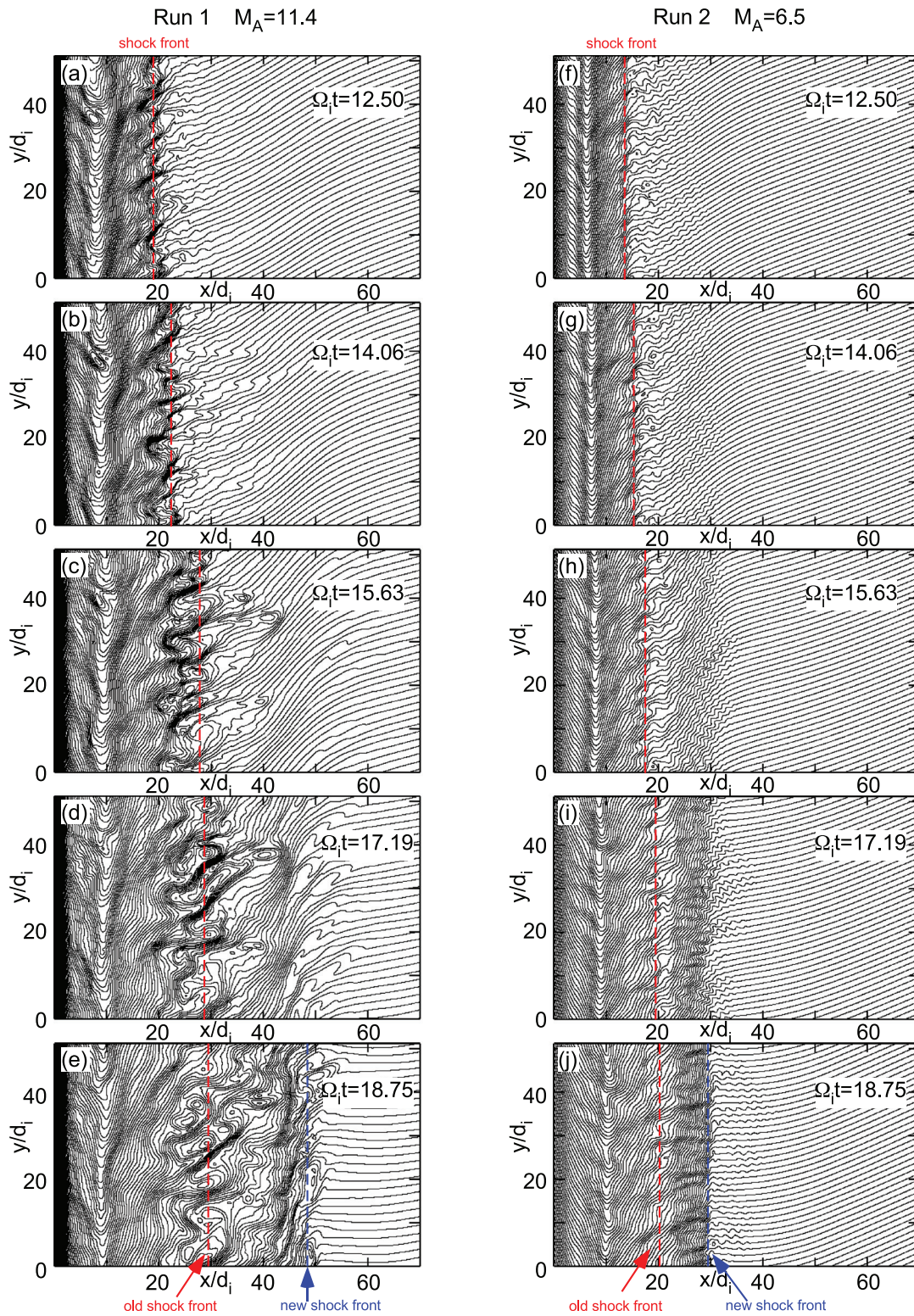


FIG. 2. Magnetic field lines projected on the x - y plane for Run 1 (a)–(e) and Run 2 (f)–(j). The time in each panel corresponds to the time in each panel in Fig. 1. The red dashed line represents the shock front at each time, and the blue dashed line in the bottom panel at $\Omega_i t = 18.75$ is the new shock front generated by the shock reformation.

blue dashed line (the new shock front) becomes the shock downstream region, which contains turbulence generated by waves excited before the new shock front is formed, and there are several magnetic islands.

The shock in Run 2 ($M_A = 6.5$) in panels (f)–(j) is much less turbulent than the shock in Run 1. In panels (f)–(h), the shock transition region (between $x = 15d_i$ to $x = 30d_i$) has winding magnetic field lines due to the instability. The wavelength of the waves is of the order of d_i , shorter than the wavelength in Run 1. As time elapses, B_y becomes larger and larger in the transition region, and the shock reformation occurs. At $\Omega_i t = 17.19$ [panel (i)], a new shock front is formed at $x = 27d_i$, and the peak of B_y in the shock front keeps growing. However, even after the formation of the new shock front, there is no magnetic island formation in the shock transition region and the downstream region [panel (j)], which is contrasted with Run 1, panel (e). Although we observed several magnetic islands during the interval from $\Omega_i t = 12.5$ to 18.75, the number of magnetic islands observed in Run 2 is much smaller than that in Run 1, and in the smaller Alfvén Mach number shock (Run 2), reconnection does not play a significant role in the shock, compared with the higher M_A run (Run 1).

Figure 3 displays the out-of-plane current density J_z for Run 1 and Run 2. The left panels (a)–(d) show the results for Run 1 ($M_A = 11.4$). At $\Omega_i t = 14.06$, there are many current sheets (red and black stripes) around the shock front ($x = 22d_i$), while the foreshock region ($22d_i < x$) has small amplitude J_z structures, as yellow and blue stripes. Consistent with these J_z stripes, magnetic field lines (black curves) are winding. At $\Omega_i t = 15.63$, around which the shock reformation starts, there are a few long current sheet structures extending from the shock front ($x = 25d_i$) toward the foreshock. These extended structures contain a few magnetic islands in the region $30d_i < x < 45d_i$. In the region $45d_i < x$, there are coherent waves propagating from the upstream toward the shock, seen as small amplitude (light green/light blue) diagonal stripes. At $\Omega_i t = 17.19$, a large island remains around $x = 40d_i$, and the magnetic fields pile up in front of the island. The waves in the foreshock region $45d_i < x$ grow to much larger amplitudes, rendering the magnetic field lines distorted more significantly than at the previous time. Along a few J_z stripes, short-wavelength waves are excited (see the region $45d_i < x < 50d_i$ and $y < 38d_i$). At $\Omega_i t = 18.75$, the new shock front is formed around $x = 45$ – $50d_i$, and there are multiple almost-vertical stripes of J_z around the new shock front. The region between the old shock front ($x = 30d_i$) and the new shock front ($x = 45d_i$) becomes the shock downstream region, and there are also complex turbulent structures of J_z in that region. The B_y pileup in front of the large magnetic island around $x = 40d_i$ becomes almost uniform in the y direction around $x = 45d_i$, and the magnetic field points almost in the y direction in the new shock front.

The right panels of Figs. 3(e)–3(h) show J_z for Run 2 ($M_A = 6.5$). Since the Alfvén Mach number in Run 2 is much smaller than that in Run 1, we see less turbulent structures in the shock, even though waves with a significant amplitude are excited. At $\Omega_i t = 14.06$, the shock front is around $x = 15d_i$, and there are structures of alternating J_z in the foreshock region $20d_i < x$. The wave planes seen in $20d_i < x < 30d_i$ are almost perpendicular to the magnetic field. In the simulation frame, these waves are propagating toward the upstream. Field lines are winding because of those waves. At $\Omega_i t = 15.63$, the amplitude of waves in the foreshock region $25d_i < x < 35d_i$ becomes larger than that in the previous time, and

some modulations appear in the direction of the wave plane. At $\Omega_i t = 17.19$, the new shock front forms around $x = 27d_i$, and the front of the waves in the foreshock ($30d_i < x$) becomes more non-uniform than at the previous time. At $\Omega_i t = 18.75$, the new shock front has a larger B_y , and the wave amplitude in the foreshock $30d_i < x$ becomes smaller than that in the previous time. During the shown interval from $\Omega_i t = 14.06$ to 18.75, only coherent waves are generated in the shock transition region, and reconnection does not play a significant role.

In the following, to discuss detailed structures of current sheets, we will show the results of Run 1 ($V_{dx} = -9v_A$). Figure 4 plots the blowups of several small regions that contain current sheets at $\Omega_i t = 18.75$. Figure 4(a) is the current density J_z in the shock including the foreshock, transition, and downstream regions, and we marked four areas, from #1 to #4 in the shock transition region, by yellow boxes, and magenta Xs represent the positions of reconnection X-lines. There are two types of current sheets: reconnecting current sheets, which have reconnection X-lines with a field-line topology change, and non-reconnecting current sheets, which do not have reconnection X-lines. In areas #1, #2, and #3, there are multiple X-lines; in contrast, area #4 does not contain X-lines. Figure 4(b) shows J_z in area #1, which has already been discussed in the previous paper.¹⁷ This area contains two X-lines, and the right X-line, at $(x, y) = (48.18d_i, 27.05d_i)$, is on the positive (red) current sheet, and readers can refer to Ref. 17 for more details about the field structures in this current sheet.

Figures 4(c)–4(e) show physical quantities in area #2: the current density J_z , the electron fluid velocity V_{ey} , and the energy conversion rate $\mathbf{J} \cdot \mathbf{E}'$, where $\mathbf{E}' = \mathbf{E} + \mathbf{V}_e \times \mathbf{B}/c$ is the electric field in the electron rest frame, respectively. In this area, there are three X-lines, and let us focus on the top two X-lines, at $(x, y) = (50.35d_i, 39.225d_i)$ and $(x, y) = (50.4d_i, 38.7d_i)$. The upper X-line is located on the negative (black) J_z current sheet [see panel (c)], while the lower X-line is located between the positive (red) current sheets. In the vicinity of the lower X-line, J_z is negative (green to light blue colors). The time evolution of the field lines (not shown) indicates that the reconnection around the lower X-line occurs between the field lines in the upper right quadrant and the field lines in the lower left quadrant, which means there is a negative current sheet J_z extending diagonally from the upper left to the lower right regions across the X-line. Panel (d) shows that V_{ey} becomes positive around those X-lines, and electron jets exist in the upper sides of the X-lines. Panel (e) demonstrates that around these X-lines and electron jets, $\mathbf{J} \cdot \mathbf{E}'$ becomes positive, although some regions along the jets have negative values.

Figures 4(f)–4(h) are the current density J_z , the electron fluid velocity V_{ex} , and the energy conversion rate $\mathbf{J} \cdot \mathbf{E}'$ for area #3, in which four X-lines are formed. Panel (f) shows that there are two magnetic islands whose centers are around $(x, y) = (49.75d_i, 30.6d_i)$ and $(x, y) = (49.7d_i, 29.6d_i)$, and J_z becomes positive in those islands. The two islands are separated due to the negative (black) current sheet, and there is an X-line at $(x, z) = (49.675d_i, 30.1d_i)$ on the negative J_z . Panel (g) shows that along this negative current sheet with the X-line, there is a negative V_{ex} flow. Above the upper island and below the lower island, there are other X-lines (the X-line below the lower island is outside of the box), around which there are also negative electron V_{ex} flows. Panel (h) demonstrates that along these negative J_z sheets and negative V_{ex} flows, $\mathbf{J} \cdot \mathbf{E}'$ features large positive values.

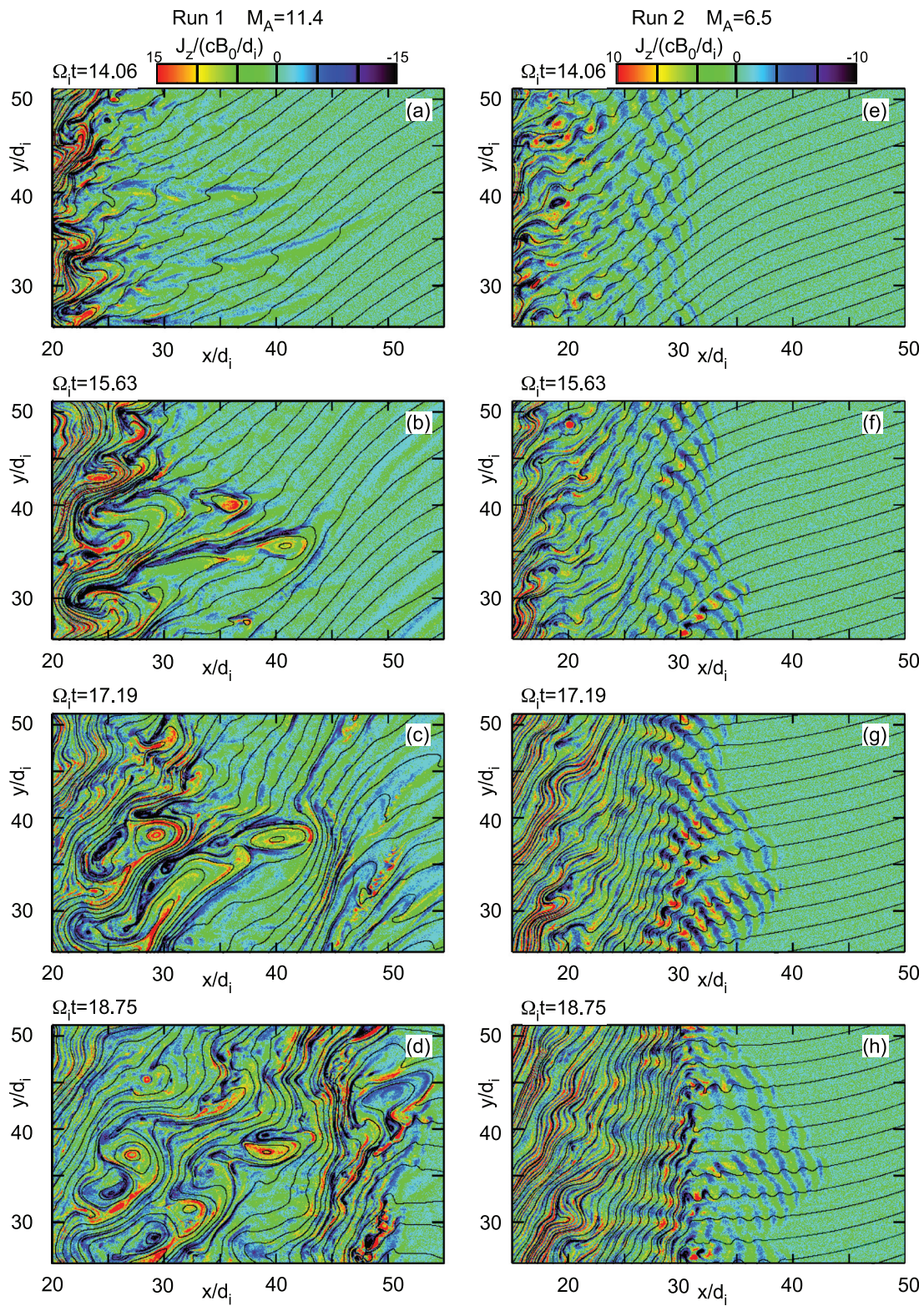


FIG. 3. Current density J_z (color) in the x - y plane for Run 1 (a)–(d) and Run 2 (e)–(h). The black curves show the magnetic field lines projected on the x - y plane.

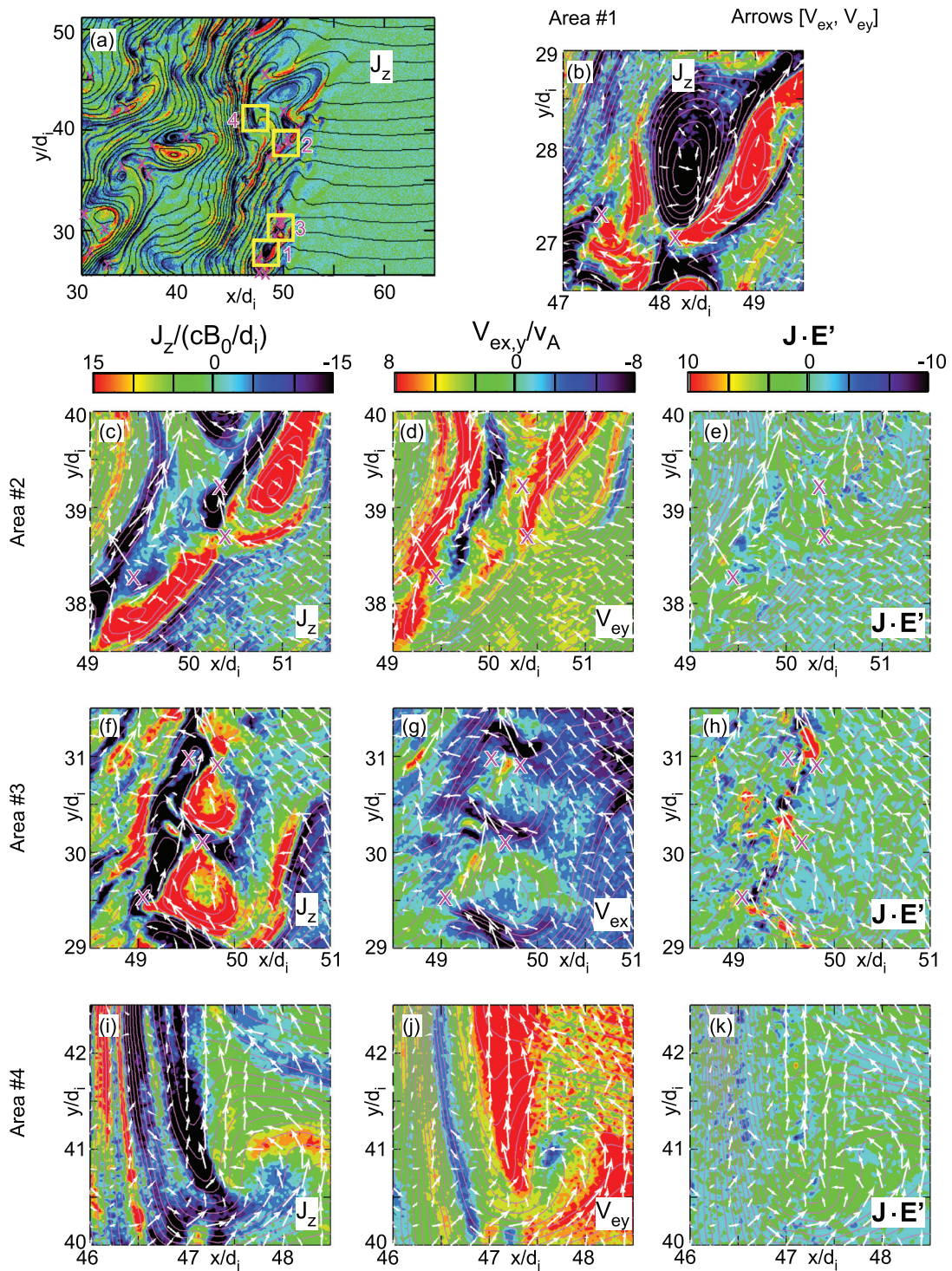


FIG. 4. (a) Current density J_z (color) for Run 1 at $\Omega_e t = 18.75$. The black curves are magnetic field lines projected on the x - y plane. Magenta Xs are the positions of reconnection X-lines. Four yellow boxes, #1 to #4, are areas where the details of current sheets are discussed. Area #1 is the same region discussed in Ref. 17, and an example of the plot J_z is given in panel (b). Panels (c)–(e) are for area #2, panels (f)–(h) are for area #3, and panels (i)–(k) are for area #4. In each area, the current density J_z , the electron fluid velocity V_{ey} or V_{ex} , and the energy dissipation rate $J \cdot E'$, where $E' = E + V_\phi \times B/c$, are plotted. Magenta lines are magnetic field lines projected on the x - y plane, magenta Xs represent the positions of X-lines, and white arrows are vectors of electron fluid velocity.

The above two areas (#2 and #3) are examples of reconnecting current sheets, where strong electron jets and positive $\mathbf{J} \cdot \mathbf{E}'$ are generated. In contrast, there are many non-reconnecting current sheets, too, and Figs. 4(i)–4(k) show such an example. Panel (i) plots J_z in non-reconnecting current sheets. There are several positive and negative J_z stripes in the vertical direction, and the magnetic field B_y reverses across the right-most negative J_z around $x = 47d_i$ (see the field lines in that current sheet). Even though B_y reverses along this negative current sheet, there is no reconnection X-line. Nonetheless, panel (j) exhibits a strong positive electron jet V_{ey} along the rightmost vertical negative current sheet. Panel (k) shows that $\mathbf{J} \cdot \mathbf{E}'$ becomes positive along that current sheet, although some regions along the current sheet have a negative $\mathbf{J} \cdot \mathbf{E}'$.

The energy conversion rate $\mathbf{J} \cdot \mathbf{E}'$ in non-reconnecting current sheets with the magnetic field reversal tends to be smaller than that in reconnecting current sheets. The magnitude of the positive $\mathbf{J} \cdot \mathbf{E}'$ in the non-reconnecting current sheet in area #4 [panel (k)] is around $5cB_0^2/d_i$ throughout the negative J_z sheet, except for a local region around $(x, y) = (47.1d_i, 41.9d_i)$ where it reaches around $10cB_0^2/d_i$. In contrast, the reconnecting current sheet in area #3 [panel (h)] shows that $\mathbf{J} \cdot \mathbf{E}'$ in these negative V_{ex} jets around the X-lines reaches $\sim 25\text{--}30cB_0^2/d_i$. In addition, the reconnecting current sheet in area #1 (see Fig. 2 in Ref. 17) shows that $\mathbf{J} \cdot \mathbf{E}'$ exceeds $15cB_0^2/d_i$. The reconnecting current sheet in area #2 [panel (e)] exhibits a little bit smaller $\mathbf{J} \cdot \mathbf{E}'$ around $7.5cB_0^2/d_i$, except for small numbers of local regions where $\mathbf{J} \cdot \mathbf{E}' \sim 10cB_0^2/d_i$. This is because the reconnection in area #2 is not fully developed at this time $\Omega_i t = 18.75$, indicated by the small magnitude of the negative J_z around the X-line at $(x, z) = (50.4d_i, 38.7d_i)$. If we consider the area average, using a square $0.5d_i \times 0.5d_i$ around the X-line, the reconnecting current sheets in area #2 and #3 show $\langle \mathbf{J} \cdot \mathbf{E}' \rangle = 0.60cB_0^2/d_i$ and $1.63cB_0^2/d_i$, respectively. In contrast, the area average around the non-reconnecting current sheet in area #4 is $\langle \mathbf{J} \cdot \mathbf{E}' \rangle = 0.31cB_0^2/d_i$.

In the following, we will investigate further each reconnecting/non-reconnecting current sheet: reconnecting current sheets with a regular bipolar jet structure (area #2), reconnecting current sheets with a one-sided jet structure (area #3), and non-reconnecting current sheets (area #4).

2. Reconnecting current sheets, area #2

In Ref. 17, a reconnection region in area #1 is analyzed, and a bipolar jet structure is shown. Area #2 contains another example of a reconnection region with a bipolar jet. Figure 5 displays the contour plots and profiles for several quantities for the reconnecting current sheet in area #2. Panels (a)–(f) show: (a) the out-of-plane magnetic field B_z , (b) electron fluid velocity V_{ex} and (c) V_{ey} , (d) electron density n_e , (e) ion fluid velocity V_{ix} , and (f) V_{iy} . Let us focus on the second top X-line at $(x, y) = (50.4d_i, 38.7d_i)$. This X-line is moving, with a velocity $[-3.00, 5.11]v_A$ in the x – y plane. These six panels plot the quantities in the reference frame where the second top X-line is stationary. In the following, we call this frame the X-line stationary frame.

Panel (a) demonstrates that there is a guide field B_z in the reconnection region (the second top X-line). The value around the X-line is $B_z \sim -3B_0$, which is almost twice larger than the reconnecting component of the magnetic field. In this X-line stationary frame, panels (b) and (c) show that the electron flow has a bipolar jet structure around

the X-line. The positive V_{ex} and V_{ey} flows around the X-line are easily recognized, especially in the V_{ey} plot [panel (c)], but there is a small localized region where V_{ex} and V_{ey} are negative [see panel (c), below the X-line], around $(x, y) = (50.2d_i, 38.5d_i)$. The arrows represent the velocity vector for the electron fluid in the X-line stationary frame. They show that there are the electron inflows from the negative x side and the positive x side toward the vicinity of the X-line, and the upward electron jet flows out from the X-line. The downward jet is weak, except for the localized region around $(x, y) = (50.2d_i, 38.5d_i)$. In panel (a), the green ovals and the red ovals indicate the electron inflows and the electron outflows around the X-line, respectively.

The electron density [panel (d)] shows that a layer with a large density is elongated diagonally in the direction from the upper right to the lower left. Panels (e) and (f) are the ion fluid velocities V_{ix} and V_{iy} , and there are only almost uniform ion flows around the X-line, from the upper right to the lower left regions. There are no ion jets from the X-line. Therefore, this is a region of electron-only reconnection,⁷ where only electrons participate in reconnection, and ions just pass through the region, similar to area #1 discussed in Ref. 17. This electron-only reconnection is also consistent with previous theoretical and numerical studies^{34–36} with a laminar electron-scale current sheet where ions are unmagnetized, and ions are not involved in reconnection physics inside the thin layer.

Panels (g)–(l) are the profiles of quantities along the yellow line in the contour panels (a)–(f), crossing the second top X-line diagonally. This yellow line is almost perpendicular to the reconnecting component of the magnetic field. Note that the magnetic fields in the first quadrant (positive x and positive y sides) around the X-line, and those in the third quadrant (negative x and negative y sides) around the X-line, are reconnecting. In the panels (g)–(l), the horizontal axes represent the x position of the yellow line. The magnetic field B_y [see panel (g)] changes from negative to positive as we move from the right to the left. The vertical dashed line in panels (g)–(l) is the position of the X-line, at $x = 50.4d_i$. The guide field B_z is around $-3B_0$ at the X-line, and its magnitude is almost twice larger than the reconnecting component of the magnetic field ($\sim 1.5B_0$) in the right side of the reconnection region, around $x = 50.6d_i$. The electric field [panel (h)] shows some fluctuations, and E_z at the X-line becomes a small negative value. The magnitude of the reconnection electric field ($|E_z|$ at the X-line) is around $0.026B_0$, from which the normalized reconnection rate is $0.15B_{dm}V_{out}/c$, where $B_{dm} = 1.35B_0$ is the magnitude of the reconnecting magnetic field in the upstream region (the mean value at the two positions, at $x = 50.2d_i$ and at $x = 50.6d_i$), and $V_{out} = 7.27v_A$ is the maximum outflow speed, $(V_{ex}^2 + V_{ey}^2)^{1/2}$, in the upward directing electron jet from the X-line. Note that we here assumed symmetric reconnection, since the magnetic field and the density profiles are almost symmetric within the region up to $0.2d_i$ away from the X-line. The reconnection electric field averaged around the X-line (using a square with its side $0.5d_i$) is $\langle E_z \rangle = -0.020B_0 \pm 0.010B_0$, where the uncertainty is due to the time fluctuation during 90 time steps. Using this value, the reconnection rate is $0.12 \pm 0.06B_{dm}V_{out}/c$. Panel (i) plots the current density, and J_z is close to zero or negative around the X-line, but $|J_z|$ is not large there. This indicates that the negative current sheet J_z around this X-line has just started to form. The time history of the reconnection in this current sheet (not shown) shows that the magnitude of the negative J_z grows as time evolves, and a clearer

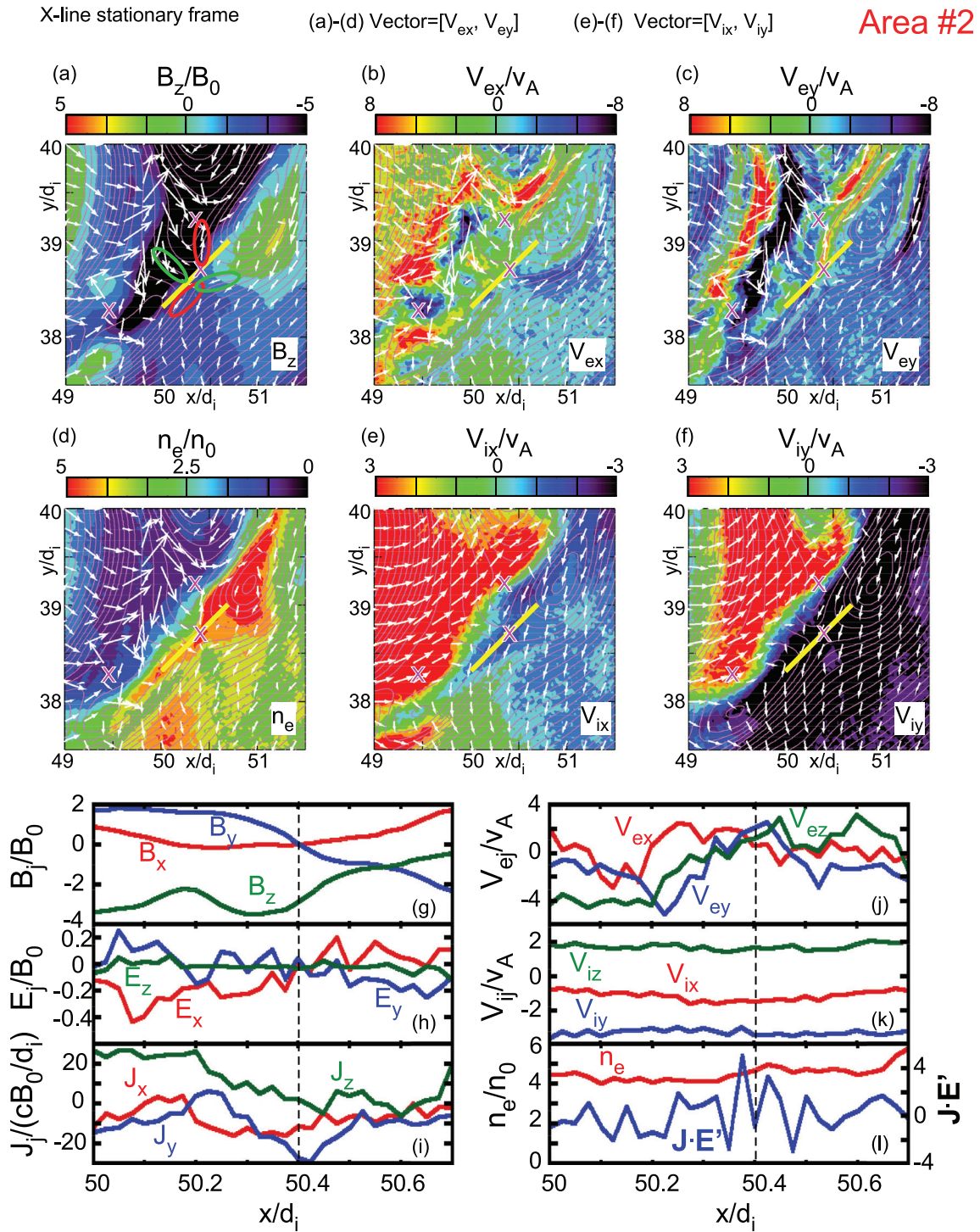


FIG. 5. Details of field structures in area #2, where there are reconnecting current sheets. (a) magnetic field B_z , (b) and (c) electron fluid velocity V_{ex} and V_{ey} , (d) electron density n_e , and (e) and (f) ion fluid velocity V_{ix} and V_{iy} . In each plot, the magenta lines are magnetic field lines projected on the x - y plane, and magenta Xs are the positions of X-lines. White arrows are velocity vectors of electron fluid velocity [panels (a)–(d)] and ion fluid velocity [panels (e) and (f)]. In (a), the green/red ovals indicate the electron inflows/outflows, respectively. In each panel, the yellow solid line on the second top X-line is the cut line across the X-line, along which the field profiles are plotted in panels (g)–(l). (g) Each component of the magnetic field, (h) electric field, (i) current density, (j) electron fluid velocity, (k) ion fluid velocity, (l) electron density (red), and the energy dissipation rate $J \cdot E'$ (blue).

reconnecting current sheet appears in a later time. This reconnection looks like driven reconnection.

The electron fluid velocities [panel (j)] show that V_{ey} is non-zero at the X-line. This is because the electron jet ($V_{ey} > 0$) is generated slightly away from the X-line, as shown in panel (c), in which the jet starts slightly below the X-line. In the negative x side of the X-line, there is a negative V_{ey} flow, because the electron flow has a bipolar jet structure around the X-line. The ion flow velocities [panel (k)] show that ion flows are almost uniform background flows. Panel (l) demonstrates that the density is almost uniform along the yellow line in the contour plots. The energy conversion rate, $\mathbf{J} \cdot \mathbf{E}'$, fluctuates along this yellow line, and it becomes positive around the X-line, although the value at the X-line is negative. The negative $\mathbf{J} \cdot \mathbf{E}'$ results partially from a small positive J_z on the X-line, instead of a negative value. Due to fluctuating J_z and the fact that reconnection is in its developing stage, no fully developed negative J_z exists around the X-line yet. However, if we average out such a fluctuation, $\mathbf{J} \cdot \mathbf{E}'$ around the X-line gives a positive value. In a later time (not shown), the negative J_z grows and the value of $\mathbf{J} \cdot \mathbf{E}'$ becomes larger.

3. Reconnecting current sheets, area #3

Reconnection sites in the shock-driven turbulence can have jet structures distinct from the regular bipolar jets (such as area #1 and #2). Area #3 contains such an example, characterized by one-sided jets. Figure 6 shows the quantities in area #3. In this area, there are two magnetic islands and four X-lines. Panel (a) plots B_z , and let us focus on the second from the bottom X-line at $(x, y) = (49.675d_i, 30.1d_i)$. The magnetic field at the X-line is $B_z \sim -4B_0$, which is almost twice larger than the reconnecting magnetic field B_x in this region. This X-line is moving with a velocity $[0.545, 5.02]v_A$ in the simulation frame. All the quantities in Fig. 6 are shown as the values in the X-line stationary frame. Panels (b) and (c) are the electron fluid velocities V_{ex} and V_{ey} , and in the vicinity of the X-line, there is a large electron jet with negative V_{ex} and positive V_{ey} . This jet is almost one directional around the X-line, and the opposite directional jet with a positive V_{ex} and a negative V_{ey} is located far away from the X-line [see the green/red ovals in (a), which indicate the electron inflows/outflows, respectively]. The electron flow patterns around the two magnetic islands show a vortex-like structure, in which the electrons moving clockwise around those two islands ($V_{ey} > 0$ in the left side of those islands, while $V_{ey} < 0$ in the right side of the islands). The electron density [panel (d)] is almost flat but there is a slight asymmetry between the top and the bottom sides of the X-line, and the density above the X-line is slightly higher than below the X-line. Ion flows [panels (e) and (f)] show that there are almost uniform V_{ix} and V_{iy} flows around the X-line.

These field structures around the second bottom X-line can also be applied to the X-line above the upper island. On the top of the upper island, there is an X line and a negative V_{ex} layer, similar to the negative V_{ex} layer above the lower island. Also, below this box, there is another X-line (not shown), and there is another negative V_{ex} layer below the lower island. In addition, the B_z structure [panel (a)] and the density structure [panel (d)] are similar in the upper and the lower islands: the lower right quadrant of each island has a positive B_z , while the upper left quadrant of each island shows a negative B_z . The density becomes high in the lower left and the bottom regions of each island.

Panels (g)–(l) are the profiles of field quantities along the yellow line across the second bottom X-line [see the yellow vertical line in panels (a)–(f)]. Panel (g) shows the profiles of magnetic field, where the reconnecting magnetic field is almost in the x direction, reversing its sign at the X-line at $y = 30.1d_i$ (the vertical dashed line). The upper side of the X-line ($30.1d_i < y$) has a larger magnetic field B_x than the lower side ($y < 30.1d_i$). Since both the magnetic field and the density exhibit asymmetry across the current sheet, let us apply the asymmetric reconnection model.³⁷ The average magnitude of the reconnecting magnetic field $B_{dm} = 2B_1B_2/(B_1 + B_2) = 1.49B_0$, where B_1 and B_2 are the reconnecting field in the upper side and the lower side, respectively, and we used the absolute values of the maximum and the minimum B_x in panel (g), i.e., $B_1 = B_{x,max}$ and $B_2 = -B_{x,min}$. The guide field $B_z \sim -4B_0$, whose magnitude is almost three times larger than the reconnecting field. The electric fields [panel (h)] fluctuate a lot, and the reconnection electric field E_z at the X-line is $E_z = -0.047B_0$, which corresponds to the reconnection rate $0.17B_{dm}V_{out}/c$, where $V_{out} = 10.4v_A$ is the maximum outflow speed $(V_{ex}^2 + V_{ey}^2)^{1/2}$ in the left side of the X-line. Using the spatially averaged E_z around the X-line (using a square with its side $0.5d_i$), $\langle E_z \rangle = -0.0045 \pm 0.017B_0$, where the uncertainty is due to the time fluctuation during 90 time steps. This area #3 contains a larger fluctuation than area #2, and the averaged E_z around the X-line in area #3 is about five times smaller than in area #2. Therefore, the high value of the reconnection rate $0.17B_{dm}V_{out}/c$ is an instantaneous local value, and the averaged reconnection rate is $0.017 \pm 0.063B_{dm}V_{out}/c$.

Panel (i) displays the current densities, and J_z has a negative value at the X-line, and the negative J_z peak is in the upper side of the X-line, $y = 30.175d_i$. In addition, J_z becomes positive in both sides across the X-line. Panel (j) plots the electron flow velocities. The V_{ey} plot exhibits no signature of the electron inflows toward the X-line, and the V_{ex} plot shows a negative flow at the X-line. This suggests that the structure of the electron flow is different from the regular reconnection picture, where the inflow V_{ey} is generated toward the X-line, and the outflow V_{ex} comes out from the X-line. Instead, the negative V_{ex} coming from the positive x side of the X-line [see panel (b) and the electron flow with negative V_{ex} covering the region around the X-line] may play a role as the inflow toward the X-line, and the one sided outflow comes out from the X-line. Panel (k) exhibits almost uniform ion flows. Panel (l) demonstrates that the electron density has small asymmetry across the current sheet, and the densities at the upper side and the lower side are $n_1 = 5.5n_0$ and $3.2n_0$, respectively, where we took the maximum and the minimum values of n_e in panel (l). Using these densities and the magnetic fields, the asymmetric model³⁷ predicts that the outflow becomes $V_{out} = [B_1B_2(B_1 + B_2)/(n_1B_2 + n_2B_1)]^{1/2}(1/4\pi m_e)^{1/2} = 12v_A$, and the observed outflow is $V_{out} = 10.4v_A$, slightly smaller than the prediction. The energy conversion rate $\mathbf{J} \cdot \mathbf{E}'$ is a positive value around the X-line. Note that Fig. 4(h) shows that $\mathbf{J} \cdot \mathbf{E}'$ in the left side (outflow side) of the X-line becomes much larger than at the X-line, and the energy conversion to electron is more significant in the outflow region than that at the X-line.

4. Non-reconnecting current sheet, area #4

Figure 7 illustrates quantities in the non-reconnecting current sheets in area #4. Let us focus on the negative J_z around $x = 47d_i$.

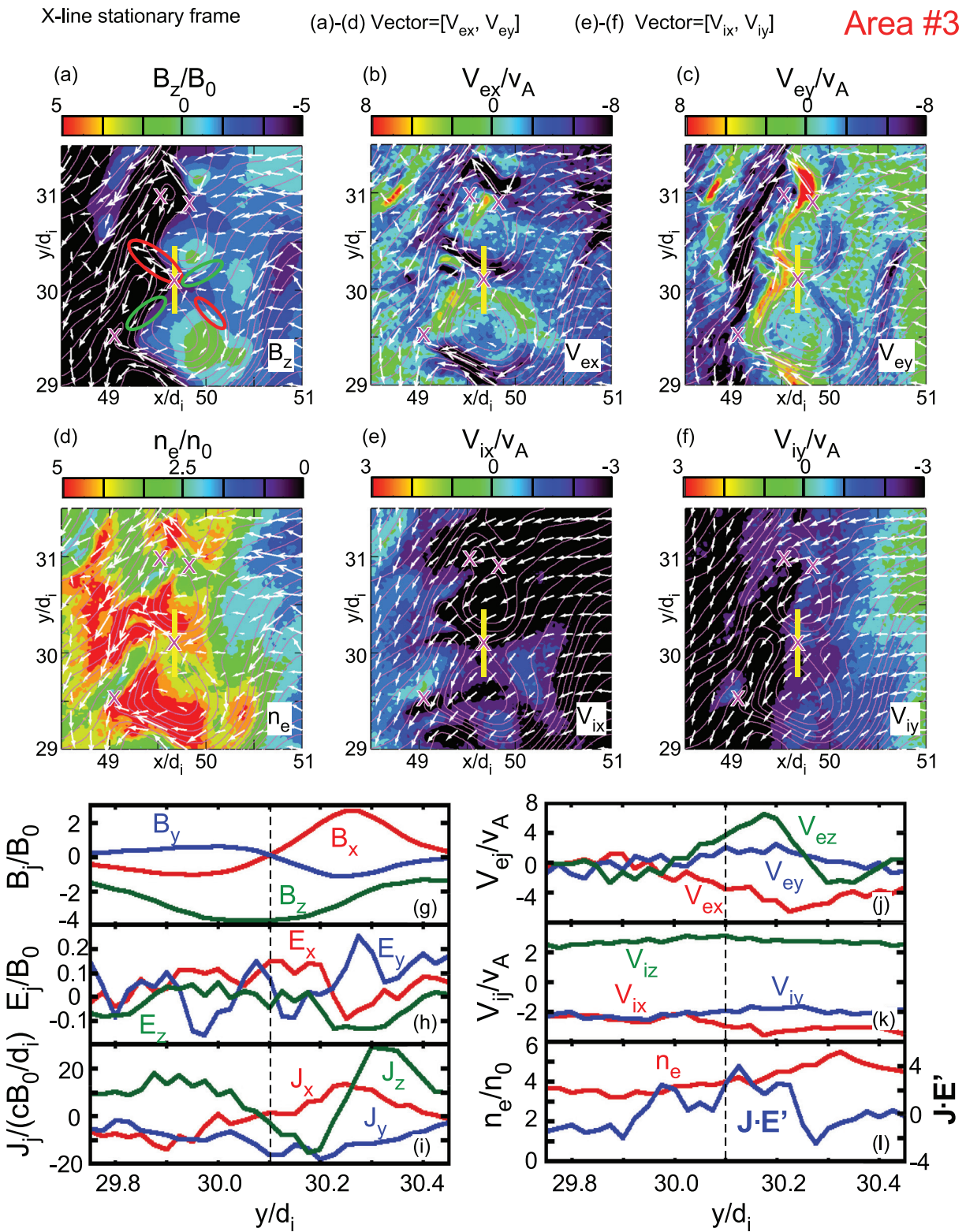
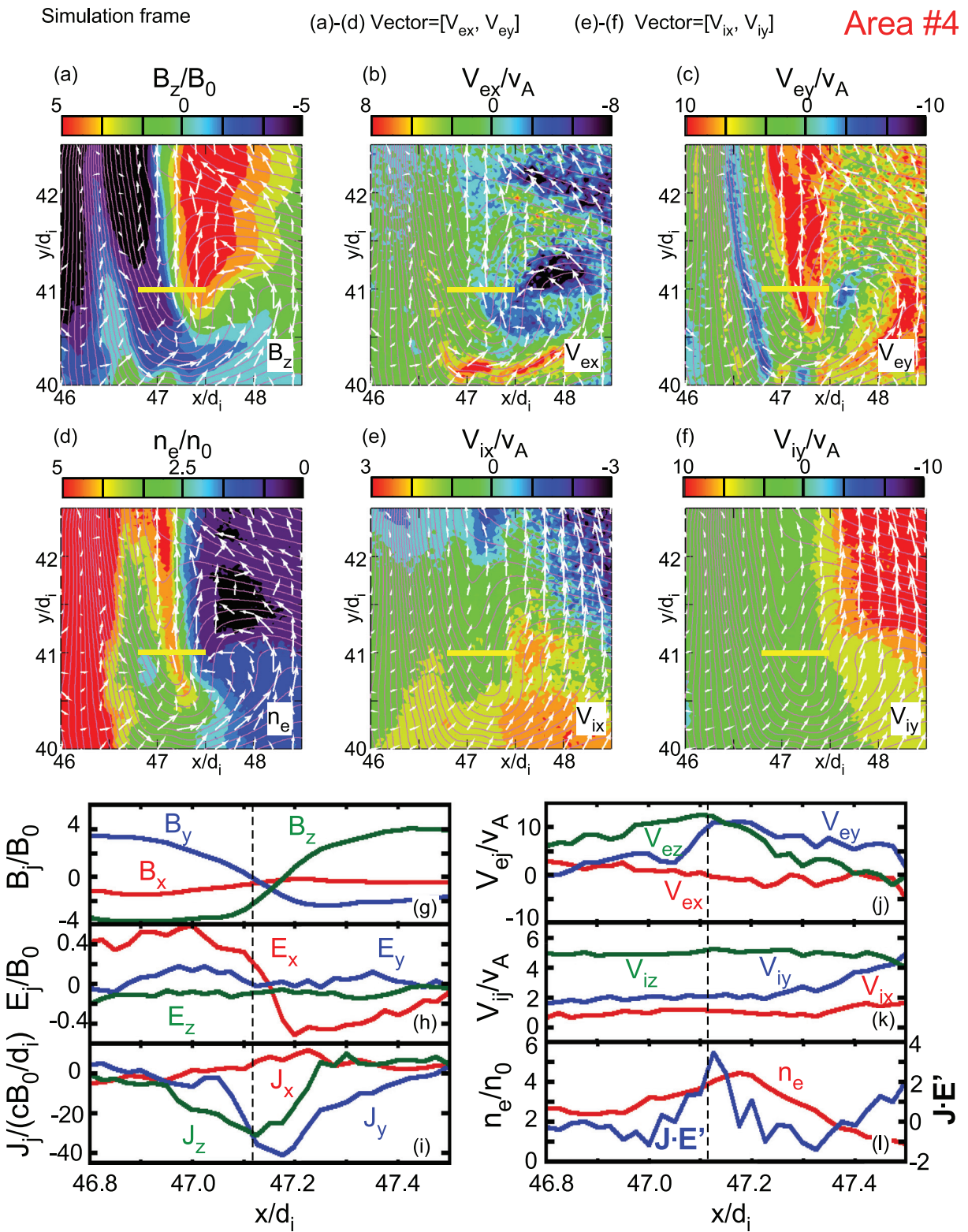


FIG. 6. 2D fields and 1D cuts for area #3, where there are reconnecting current sheets, the same format as Fig. 5.



Since there are no X-lines in this region, the quantities are shown in the simulation frame. Panel (a) demonstrates that along the non-reconnecting current sheet, B_z is negative in the left side and positive in the right side. The reversal of B_z is because there is an electron jet V_{ey} , which is seen in pane (c). Panels (b) and (c) are the electron fluid velocities, and there is an electron jet in the y direction along the current sheet. The maximum $V_{ey} \sim 13v_A$ in the jet. Electron density [panel (d)] shows an enhancement along the current sheet. Panels (e) and (f) are the ion fluid velocities. There is y directional ion flows, but no ion jet is formed associated with the current sheet around $x = 47d_i$.

Panels (g)–(l) display the profiles of field quantities across the yellow line [see panels (a)–(f)]. Panel (g) shows that B_y reverses at $x = 47.11$ (the dashed line), and B_z also changes its sign around the dashed line. Panel (h) plots the electric fields. The signs of the electric fields are consistent with the signs of $-\mathbf{V}_e \times \mathbf{B}/c$ (not shown), although the electrons are unmagnetized in this area and $\mathbf{E} \neq -\mathbf{V}_e \times \mathbf{B}/c$: the electric field E_x reverses its sign across the current sheet, and E_z becomes almost uniformly negative because of the positive V_{ey} flow and the negative B_x across the current sheet.

Panel (i) shows that J_z becomes negative, and at the same time J_y becomes negative due to the strong V_{ey} flow. Panel (j) displays the electron fluid velocities, and both V_{ey} and V_{ez} become positive, and $V_{ex} \sim 0$. Panel (k) shows that the ions have almost uniform flows. Panel (l) shows that the electron density has an enhancement around the current sheet. The energy conversion rate $\mathbf{J} \cdot \mathbf{E}'$ becomes positive in the current sheet, and the peak of $\mathbf{J} \cdot \mathbf{E}'$ is near the B_y reversal (dashed line). Note that as seen in Fig. 4(k), the magnitude of $\mathbf{J} \cdot \mathbf{E}'$ is almost uniformly $5cB_0^2/d_i$ along the current sheet, and this value is much smaller than $\mathbf{J} \cdot \mathbf{E}'$ in area #3, which reaches around $30cB_0^2/d_i$ in the downstream jet region of the second bottom X-line in area #3.

As this example reveals, non-reconnecting current sheets are also the region where the field energy is converted to particles' energy, because $\mathbf{J} \cdot \mathbf{E}' > 0$. There can be a magnetic field reversal across a non-reconnecting current sheet, and also an electron jet can be formed, which is not the result of magnetic reconnection. Note that panels (g) to (l) exhibit a similarity between this non-reconnecting current sheet and a rotational discontinuity, in which the direction of the magnetic field rotates across the current sheet. There is an electron jet between the two sides of the current sheet, and the rotational discontinuity-like structure in this current sheet region dissipates energy with a smaller energy conversion rate than reconnecting current sheets.

B. Kinetic waves excited in the shock transition region

In the shock transition region, waves are excited due to interactions between incident particles and reflected particles, as well as multiple components of beams, which eventually make magnetic field lines winding and many current sheets form.

Figure 8 exhibits the field lines (gray curves) and the current density J_z (color) at two different times. At $\Omega_i t = 15.63$, the shock front is located at $x = 27d_i$, and panel (a) shows the foreshock region. There are wave structures seen as stripes of positive (red–yellow) and negative (blue–black) J_z in the region $40d_i < x < 65d_i$. The wavelength is around $3d_i$, indicated by the two magenta lines drawn along the two crests of the wave near $x = 57d_i$. From the time sequence of J_z (not shown) in the simulation frame, in which the shock front is moving

toward the positive x direction with a speed around $2\text{--}3v_A$, we found that the waves are propagating toward the shock (in the negative x direction), obliquely to the magnetic field. The propagation angle between the wave vector (perpendicular to the wave plane) and the quasi-static magnetic field in the $x\text{--}y$ plane is between 100° and 110° . For example, when we measure the propagation angle at $x = 60d_i$, the wave vector points almost 110° from the direction parallel to the magnetic field, and the propagation angle is 103° when we measure at $x = 55d_i$. In the simulation frame, the phase speed is around $6v_A$ during the time interval from $\Omega_i t = 15.63$ to 17.19. Based on the three components of the magnetic field pattern (not shown), the polarization of the wave is right-handed in the simulation frame. The wave frequency in the simulation frame is around $13\Omega_i$. As time evolves, the wave amplitude grows, and at $\Omega_i t = 17.19$ [panel (b)], field lines (gray curves) have many winding structures. In panels (c)–(e), the diagrams illustrate the relationship between positive and negative J_z values and crests and troughs of winding magnetic field lines. Since the wave propagates obliquely to the magnetic field, magnetic field lines are bent where there are positive and negative J_z . Eventually, as the wave grows, the bent magnetic field lines can reconnect, as in panel (e), after two oppositely directed magnetic field lines come into contact.

In Fig. 8(b) at $\Omega_i t = 17.19$, there is another type of waves, whose wavelength is much shorter than $3d_i$. Examples of such waves are seen in the regions marked by the white ovals in panel (b). For example, in the bottom white oval, along the right red stripe, there are many sub- d_i wavelength phase fronts, and the white two lines represent one wavelength in those short-wavelength waves. Also, in the middle white oval in panel (b), along the red stripe, similar short-wavelength structures are seen. The wavelength in those regions is around $0.7d_i$, and this short-wavelength mode is generated almost along the wave plane of the long-wavelength mode whose wavelength $\lambda \sim 3d_i$.

Figure 9 plots the current density J_z , showing the time evolution of the long-wavelength mode ($\lambda \sim 3d_i$, in the following, we denote it as the LW mode) and the short-wavelength mode ($\lambda \sim 0.7d_i$, in the following, we denote it as the SW mode) in a local region, $45d_i < x < 55d_i$ and $27d_i < y < 37d_i$. In panel (a), LW modes are seen as diagonal yellow and blue stripes, and one crest ($J_z > 0$) is marked by the white line. Around this white line, the black curves are magnetic field lines projected on the $x\text{--}y$ plane, covering one wavelength of the LW mode. Note that in this region at this time $\Omega_i t = 16.66$, there is a large non-uniform $|B_z|$ up to $5B_0$ (not shown), because of the shock reformation. This makes the foreshock region eventually the new shock front. Then, the wave propagation angle changes to closer to 90° because the magnetic field $B_z \gg B_x$ and B_y , when the wave vector is in the $x\text{--}y$ plane. Along this marked crest of the LW wave (indicated with the white line), there are SW wave patterns shown as red/yellow and blue/dark-blue stripes. Two crests of the SW mode are marked by the short magenta lines. The whole wave structure of the SW mode is moving together with the motion of the crest of the LW mode, suggesting that the SW mode is propagating along the wave plane of the LW mode in the reference frame where the LW mode is stationary. Let us call this frame the LW wave frame. However, the wave plane of the SW mode (magenta line) is not perpendicular to the wave plane of the LW mode (white line), and the angle between the wave vectors (perpendicular to the wave planes) of those two modes is 143° .

Figure 9(b) displays the plot at $\Omega_i t = 17.16$. At this time, the crest of the LW mode with the white solid line is shifted leftward. The

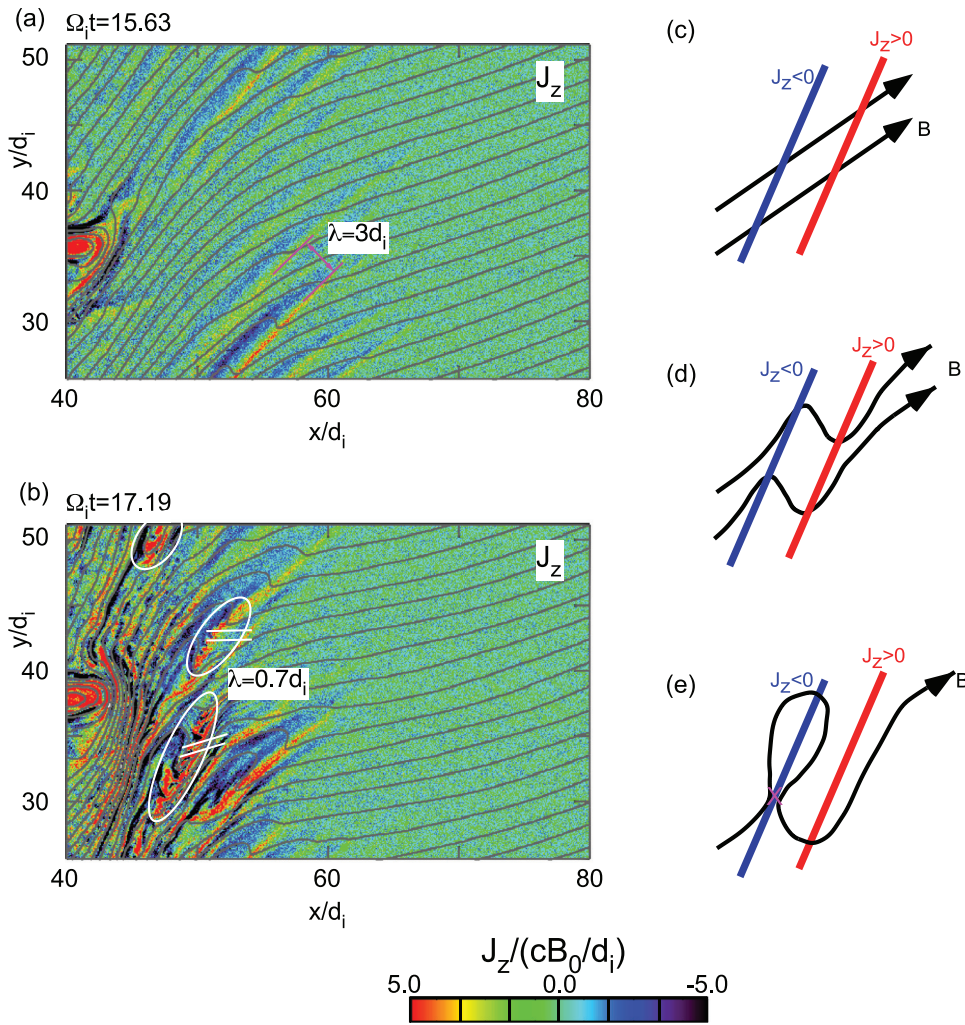


FIG. 8. (a) Current density J_z (color) at $\Omega_i t = 15.63$ and (b) J_z at $\Omega_i t = 17.19$. Gray curves are magnetic field lines projected on the x - y plane. Panel (a) shows waves whose wavelength is $3d_i$. In panel (b), white oval areas are regions where shorter wavelength waves whose wavelength is $0.7d_i$ are observed, and two crests of waves are shown by the white solid lines in the middle and the bottom oval regions. (c)–(e) diagrams illustrate how magnetic field lines are bent as the wave grows. Black arrows are magnetic field lines, and the blue and red lines show negative and positive J_z , respectively. In panel (e), the magenta X is the position where two opposite directional magnetic field lines contact and magnetic reconnection occurs.

white dashed line in the right is the original position of the crest at $\Omega_i t = 16.66$. The yellow arrow pointing from the white dashed line to the white solid line is the direction of the LW mode propagation. This arrow is parallel to the wave vector of the LW mode, which is perpendicular to the wave plane between $\Omega_i t = 16.66$ and 17.16 , the phase speed of the LW wave is $5.9v_A$. The short magenta lines on the white dashed line are the original positions of the SW mode, the same as in panel (a). These wave planes are propagating downward along the crest of the LW mode, and the short magenta lines on the solid white line are the positions of the same crests of the SW mode at $\Omega_i t = 17.16$. The magenta arrow represents the direction of the propagation of these wave planes of the SW mode in the simulation frame. If we assume that the SW mode is propagating along the wave plane of the LW mode in the LW wave frame, we can consider that the wave front motion of the SW mode in the simulation frame is the combination of motion of the crest of the LW mode (yellow arrow, from the white dashed line to the white solid line) and the wave propagation of the SW mode along the wave plane of the LW mode (dashed yellow arrow). In other

words, the dashed yellow arrow represents the phase velocity (along the wave plane of the LW mode) of the SW mode in the LW wave frame, and the phase speed in that reference frame is $4v_A$.

Due to those waves, reconnection X-lines are generated. Focusing on the region around the white solid line in panel (b), there are two types of X-lines: one is due to the LW mode, which is denoted by the blue X-line, located at $(x, y) = (47.475d_i, 32.875d_i)$, above which a d_i -scale magnetic island is seen. The other is due to the SW mode, denoted by the red X-lines right to the white line. The SW mode generates multiple sub- d_i to d_i -scale magnetic islands.

To understand the wave excitation mechanisms, we investigate electron and ion distribution functions in the region where those wave modes are observed. Figure 10 exhibits the distribution functions at locations from #1 to #4 at $\Omega_i t = 15.63$, at which time the LW mode is observed in the shock transition region. Location #1, at $(x, y) = (70d_i, 40d_i)$ is in the region where no LW waves are observed, while location #2, at $(x, y) = (60d_i, 40d_i)$, is in the region where LW waves are seen as stripes in the current density J_z [panel (a)] and the electron density n_e [panel (b)]. Location #3, at $(x, y) = (55d_i, 40d_i)$, and

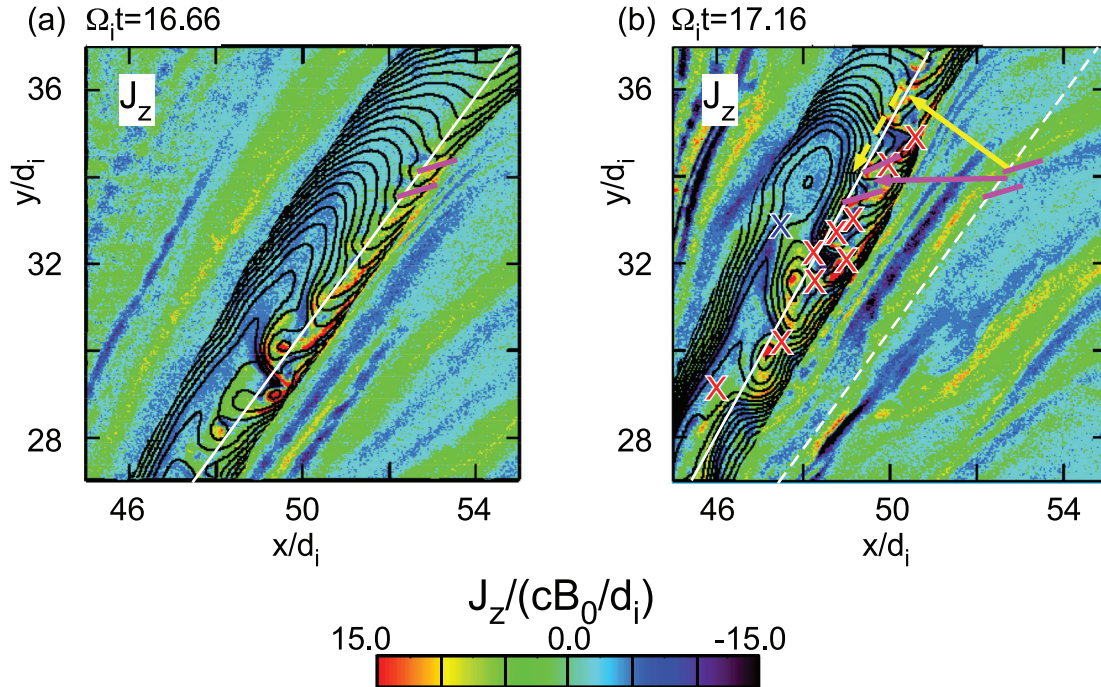


FIG. 9. (a) Current density J_z (color) at $\Omega_i t = 16.66$ and (b) at $\Omega_i t = 17.16$. In panel (a), the white solid line represents one crest of the LW (long-wavelength) wave, and black curves are magnetic field lines projected on the x - y plane for the region of one wavelength of the LW mode including one crest and one trough of the wave. Along the white line, the SW (short-wavelength) mode is excited, and the short magenta lines represent the positions of crests of the SW mode. In panel (b), the white solid line is the crest of the LW mode at $\Omega_i t = 17.16$ propagated from the original position of the short magenta line on the white dashed line at $\Omega_i t = 16.66$. The short magenta lines on the white solid line are the crest positions of the SW mode at $\Omega_i t = 17.16$ propagated from the original position of the short magenta line on the white dashed line at $\Omega_i t = 16.66$. The magenta arrow illustrates the phase velocity of the SW mode. This magenta vector is considered the sum of the solid yellow vector, which is the phase velocity of the LW mode, and the dashed yellow vector, which is the phase velocity of the SW mode in the LW wave frame. The blue X shows the reconnection X-line generated due to the LW mode, while magenta Xs are the reconnection X-lines due to the SW mode.

location #4, at $(x, y) = (55d_i, 30d_i)$, are also where LW waves are observed, and larger amplitude waves are seen at location #4. At each of the four locations, we collected particles in a square region around the location, with its side length $0.1d_i$, for ten time steps ($\sim 2.5\omega_{pe}^{-1}$), and we generated the distribution functions of electrons and ions. Panels (c1)–(c3), (d1)–(d3), (e1)–(e3), and (f1)–(f3) are for electron distribution functions for locations #1, #2, #3, and #4, respectively, and panels (c4)–(c6), (d4)–(d6), (e4)–(e6), and (f4)–(f6) are for ion distribution functions at each location. Each panel shows a reduced distribution function, in which the particle count is integrated along the velocity component perpendicular to the 2D velocity components in each panel. The white dashed arrow represents the projection of the magnetic field direction in each 2D velocity plane.

Panels for locations #2 and #3, where LW waves are observed, show the following characteristics of the electron and ion distribution functions: Electron distribution functions in (d1) and (e1), in the v_z - v_y plane, exhibit an almost circular shape, and panels (d2) and (e2), in the v_z - v_x plane, and panels (d3) and (e3), in the v_y - v_x plane, show that the distribution function has a peak around $v_x = -17.5v_A$. In contrast, ion distributions in (d4)–(d6) for location #2 and in (e4)–(e6) for location #3 have cold incident ions (lower red dot) and reflected ions (upper diffuse component). The incident component has a peak of the distribution function at $(v_x, v_y, v_z) = (-8.5v_A, 0.5v_A, 1.5v_A)$ in location #2.

Compared with locations #2 and #3, where LW waves are observed, the ion distribution function at location #1, where LW waves are not observed, has less numbers of particles in the reflected component, and these ions are separated from the cold incident component farther in the v_x direction than those in locations #2 and #3. The growth of the LW mode is likely due to the interactions between the incident ions, the reflected ions, and the single electron beam. In location #1, the LW mode is not growing because the number of reflected ions is small.

Location #4 is in the region where the strongest LW mode is observed [see panels (a) and (b)]. In this location, larger numbers of reflected ions are seen in the ion distribution functions in (f4)–(f6), although the density at location #4 is less than that in location #3 [see panel (b)]. The large fraction of the number of reflected ions compared with the incident ions may cause the increase in the growth rate of the LW mode, resulting in the larger amplitude of the LW mode in location #4 than in location #3.

Figure 11 shows the same format of plots of electron and ion distribution functions for later time, at $\Omega_i t = 16.66$. We selected four locations: Location #1 is where LW waves are observed, but no SW waves are seen. Location #2 is where SW waves are observed on top of a crest of the LW wave. Location #3 is where a significant amplitude of SW waves and distorted field lines is observed. Location #4 is next to

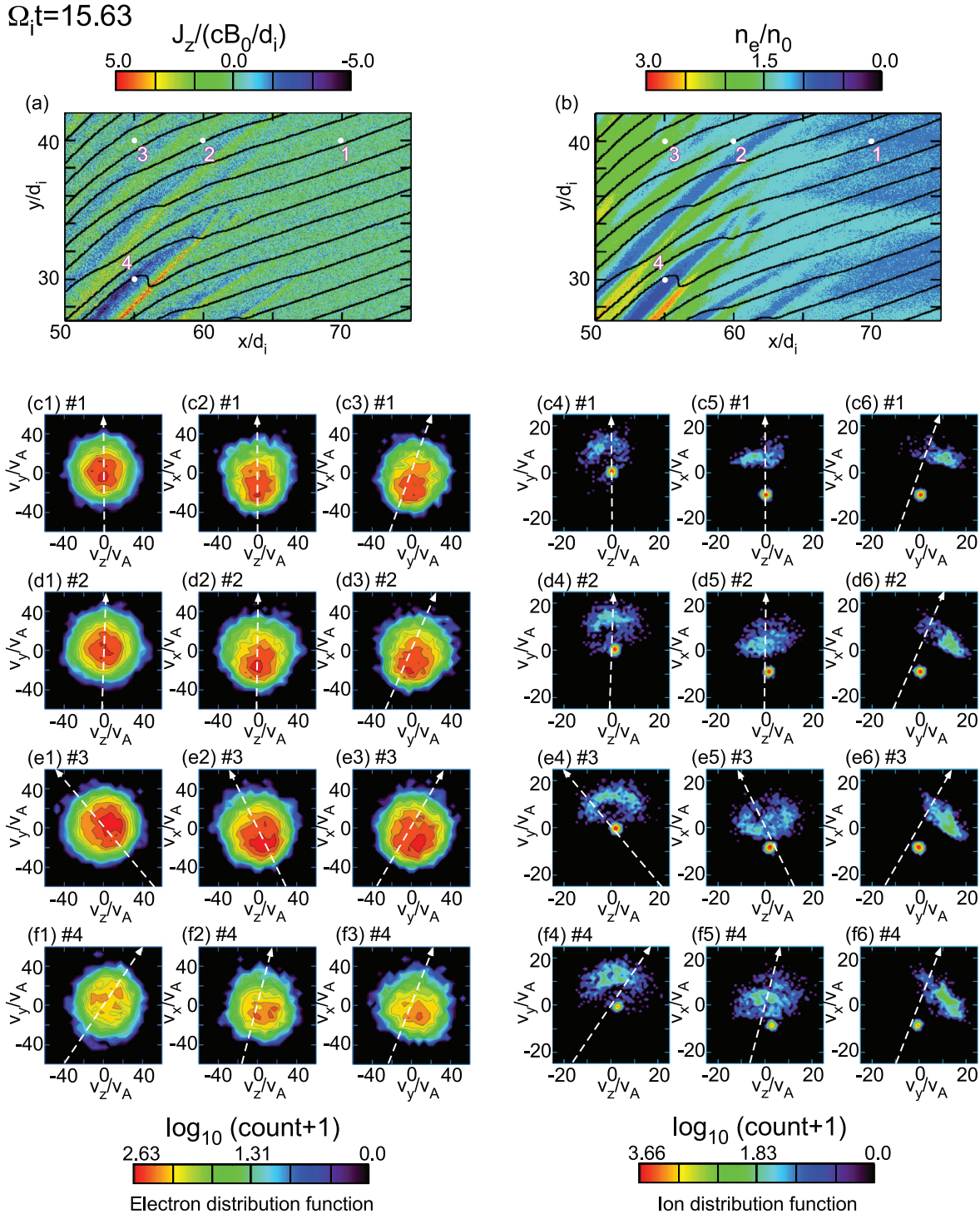


FIG. 10. (a) Current density J_z (color) and (b) electron density (color) at $\Omega_i t = 15.63$. Black curves are magnetic field lines projected on the x - y plane. The white dots, #1 to #4, are the positions where the electron and ion distribution functions are measured. Location #1 is where no LW mode is observed. Locations #2 to #4 are where LW waves are generated. Location #4 is where the largest LW waves are observed. (c1)–(c3) are the electron distribution functions and (c4)–(c6) are the ion distribution functions in location #1. Each panel shows the reduced distribution function in which particle counts are integrated in the velocity component perpendicular to each 2D velocity plane. White arrows are the projection of the magnetic field direction in each velocity plane. The same format for (d1)–(d6) for location #2, (e1)–(e6) for location #3, and (f1)–(f6) for location #4.

the SW wave turbulence, but it is where SW wave activity is quiet and only LW waves are seen. Panels (c1)–(c3) and (c4)–(c6) are for location #1, and they exhibit similar distribution functions to those in Figs. 10(d1)–10(d3) and 10(d4)–10(d6), respectively, where only LW waves are observed.

Panels (d1)–(d3) in Fig. 11 are the electron distribution functions in location #2, where small-amplitude SW waves are observed along the crest of the LW wave. In these panels, there are multiple components of electron beams. Ion distribution functions in panels (d4)–(d6) show distributions similar to those in location #1, with a cold core and the reflected ions. Therefore, SW waves are attributed to multiple beam components in both electrons and ions, i.e., electron beams seen in panels (d1)–(d3) and ion beams in panels (d4)–(d6).

Location #3, where the strongest SW wave turbulence is observed, has more outstanding electron beam structures in panels (e1)–(e3). The contour lines in panels (e1)–(e3) show outstanding two electron beam components. The strong SW turbulence is likely driven by these electron beams. Ion distributions (e4)–(e6) have similar structures to those in locations #1 and #2.

In contrast, in the electron distributions in location #4, panels (f1)–(f3), where only strong LW waves are generated, there are no clear electron beam components, and the distributions are more similar to panels (c1)–(c3) for location #1, than to distributions for location #2 and #3, although the distribution (f1) shows slight anisotropy compared to (c1). Again, ion distribution functions (f4)–(f6) are similar to those in locations #1 to #4.

IV. DISCUSSIONS AND CONCLUSIONS

We have studied magnetic reconnection in quasi-parallel shocks whose shock angle is 25° , by means of two-dimensional full PIC simulations, using parameters relevant to the Earth's bow shock. We have compared a low Mach number shock and a high Mach number shock, and have found that the number of reconnection sites increases as the Mach number increases. In the low Mach number shock ($M_A \sim 6$), waves whose wavelength is $1d_i$ are excited in the shock transition region. No strong turbulence is generated in the shock transition region, and a small number of magnetic reconnection sites are observed in the shock transition and downstream regions. In contrast, in the high Mach number shock ($M_A \sim 11$), waves whose wavelengths range from $\sim 3d_i$ to sub- d_i are excited in the shock transition region, and strong turbulence is generated as those waves interact with the shocked particles and fields.

We have investigated the properties of shock-driven magnetic reconnection in the high Mach number shock. In the shock transition region, there are several sub- d_i to d_i -scale magnetic reconnection sites in which only electrons participate in the reconnection, and ions are just passing through the X-line. There are many such small-scale reconnection sites where only a one-sided electron jet is generated, which lacks the electron jet in the opposite direction across the X-line. The reconnection rates in reconnecting current sheets have been measured, and they are around 0.1 to 0.2 based on the local values of E_z , and 0.02 to 0.1 based on the spatial averages of E_z . Note that around the reconnection X-lines, the reconnection electric field gives the dominant force to accelerate particles in the z direction, compared with the magnetic force ($-eV_e \times \mathbf{B}/c$), and the electric force in area #2 is twice larger than the magnetic force, and the electric force in area #3 is an

order of magnitude larger than the magnetic force, at $\Omega_i t = 18.75$ in the simulation.

There are also non-reconnecting current sheets, some of which show the reversal of magnetic field across the current sheet without magnetic reconnection. Both reconnecting current sheets and non-reconnecting current sheets can dissipate magnetic energy into thermal and kinetic energies of plasma; therefore, even non-reconnecting current sheets can have electron jets, and the magnetic field reversal with an electron jet and a positive energy dissipation, i.e., $\mathbf{J} \cdot \mathbf{E}' > 0$, does not necessarily mean that reconnection is occurring. Comparing the magnitude of $\mathbf{J} \cdot \mathbf{E}'$ between reconnecting current sheets and non-reconnecting current sheets, we have found a tendency that non-reconnecting current sheets with the magnetic field reversal show smaller $\mathbf{J} \cdot \mathbf{E}'$ than reconnecting current sheets.

We have studied the kinetic physics of waves excited in the high Mach number shock. In the shock transition region, waves whose wavelengths $\sim 3d_i$ (LW modes) are first excited, propagating obliquely to the magnetic field, generating current sheets. As these waves grow, magnetic field lines are bent, and magnetic reconnection sites are generated after the oppositely directed magnetic field lines come into contact. Short-wavelength ($\lambda \sim 0.5d_i$ to $1d_i$) waves (SW modes) are excited along the wave plane of the LW mode, and sub- d_i to d_i -scale small reconnection regions are generated as these SW modes grow. We have investigated electron and ion distribution functions in the shock transition region where LW modes and SW modes are excited. In regions with LW waves, electron distribution functions exhibit a single-peaked shape, while ion distribution functions show a cold incident ion component and a reflected ion component. It is expected that these two ion beams and a single-peaked electron beam destabilize LW modes. In regions with LW waves and SW waves, electron distribution functions have multiple electron beams. Ion distributions show the ion core component and the reflected ion component. It is expected that these multiple electron beams are interacting with multiple ion beams to excite SW waves.

Further studies of kinetic instabilities for LW modes and SW modes, such as analyses of the growth rates and the dispersion relations of those modes, remain to be conducted to understand the properties of excited waves, which are responsible to generate reconnecting/non-reconnecting current sheets. The LW wave we have observed in the simulation may be consistent with ion-ion beam modes observed in the Earth's bow shock,^{38–40} which are due to the incident ions and the reflected ions. Since we use an artificial mass ratio (200) in the PIC simulation, the wavelength ($\sim 3d_i$) of the LW wave observed in the simulation may vary in a simulation with a more realistic mass ratio.

In the simulation, we have observed that the LW waves are right-handed and propagating toward the shock in the simulation frame. To identify the type of the wave, the wave phase velocity in the plasma rest frame needs to be considered. According to the plasma bulk velocity in the region $50d_i < x < 55d_i$ at $\Omega_i t = 15.63$, the LW waves are propagating in the negative x direction in the plasma rest frame, opposite to the reflected ion component. If we analyze the phase speed $55d_i < x$, the LW waves propagate with almost the same velocity as the plasma bulk velocity, and it is hard to determine whether the LW waves propagate in the negative x direction in the plasma rest frame, because of uncertainties in the wave phase velocity and the plasma bulk velocity in the simulation frame. Considering the analysis in the

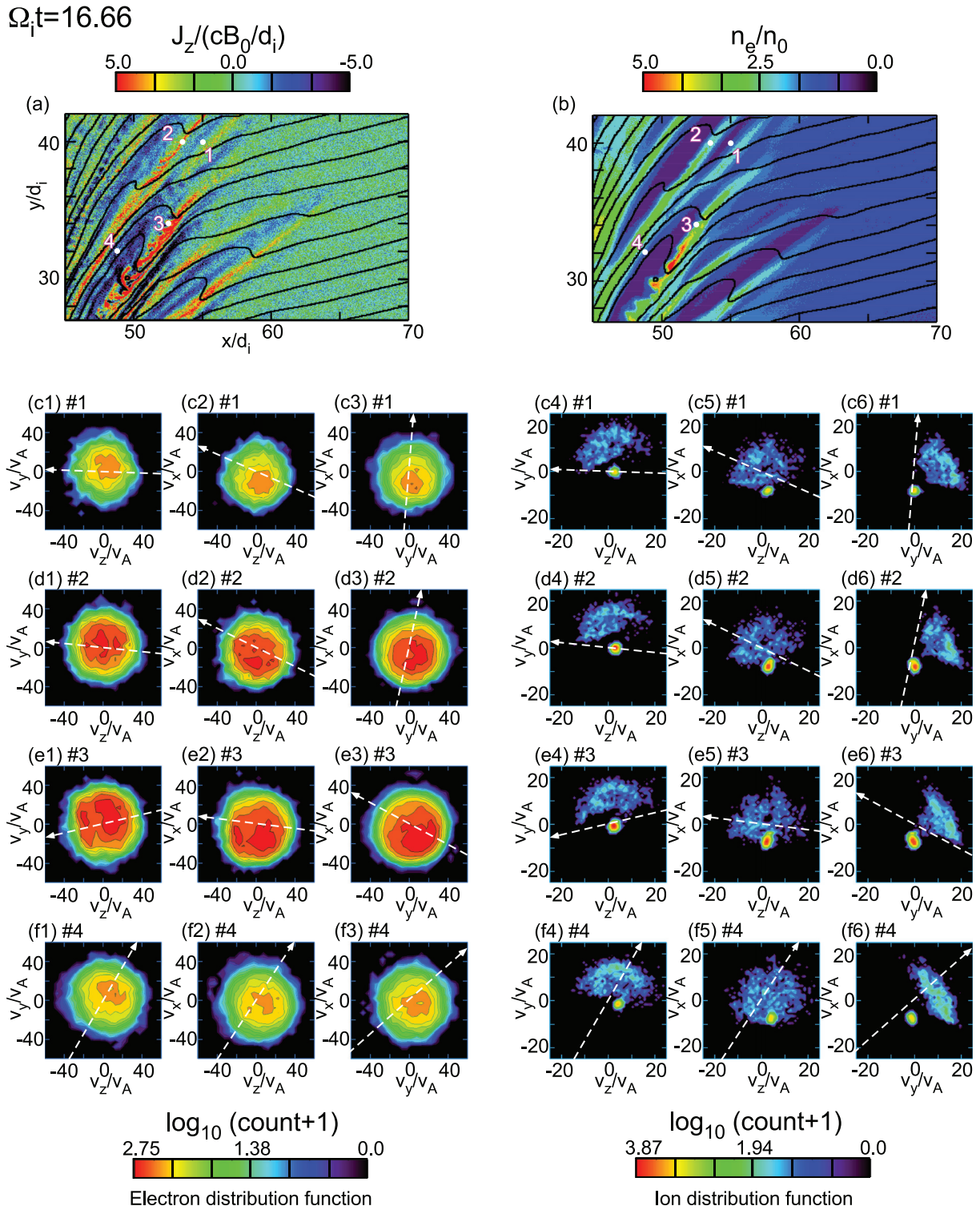


FIG. 11. Electron and ion distribution functions at $\Omega_i t = 16.66$, the same format as Fig. 10. Location #1 is where only LW waves are observed. Location #2 is where both LW waves and SW waves are observed. Location #3 is where strong SW waves are observed. Location #4 is where LW waves are observed but no significant SW waves are observed.

region $50d_i < x < 55d_i$, it is likely that the LW waves excited in this simulation are propagating toward the shock in the plasma rest frame, and we consider that the LW modes are due to non-resonant ion–ion beam instability,¹⁸ which are right-handed waves propagating away from the reflected ion component.

The SW modes we have observed in the simulation are more complicated, but one of the features of the electron distribution function in the SW mode region is outstanding two electron beams. We analyzed the wave phase velocity and the polarization in the plasma rest frame in the SW mode region in Fig. 11, around location # 3. In the plasma rest frame, the SW waves are propagating in the negative y direction along the LW wave plane, and the polarity is right-handed. The wave frequency in the plasma rest frame is estimated to be around $25\text{--}40 \Omega_i$ ($0.13 - 0.2 \Omega_e$ in the simulation where the mass ratio is 200). These results indicate that the SW waves can be whistler waves, excited under multiple electron and ion beams. Since the LW mode contains the longitudinal electric field, which generates the density fluctuations seen in Fig. 10, there exists an electric field component parallel to the magnetic field, which accelerates electrons. The electron beams accelerated within the LW waves can be the source of the secondary instability to generate whistler waves.^{41,42} The electron distributions observed in the SW modes also resemble electron distributions in modified two stream instabilities (MTSIs),^{43,44} which can generate oblique whistler waves with frequencies near the lower hybrid frequency, $0.07 \Omega_e$ in the simulation with the mass ratio of 200, although the waves by MTSIs have been discussed in quasi-perpendicular shock waves.^{45,46} As shown in Fig. 3, as time evolves, the magnetic field lines in the shock become close to the quasi-perpendicular condition, even though the upstream field lines are fixed to be a quasi-parallel condition. Therefore, waves similar to the ones excited in quasi-perpendicular shocks might operate in the turbulent quasi-parallel shock region. More investigations of wave properties and instability mechanisms are necessary, by performing linear dispersion analyses using the ion and electron distribution functions obtained in the simulations.

The above results are useful to guide the search of reconnecting current sheets and to understand the properties of magnetic reconnection driven by shocks in the Earth's bow shock region by space measurements. An abundance of current sheets has been observed in the Earth's bow shock by NASA's MMS measurements, and many of these are potential reconnection sites. Magnetic field reconstruction methods^{47–49} are available to see the magnetic field topology to determine whether observed current sheets are reconnecting or non-reconnecting. Further studies of magnetic reconnection in the Earth's bow shock are needed to understand the roles of reconnection in contributing to shock heating and particle acceleration.

ACKNOWLEDGMENTS

This work was supported by DOE Grant No. DESC0016278, NSF Grant Nos. AGS-1619584 and AGS-1552142, NASA Grant No. 80NSSC18K1369, and the NASA MMS project. This work was partially supported by the International Space Science Institute's (ISSI) International Teams programme. Work at the University of Bergen was supported by the Research Council of Norway/CoE under Contract No. 223252/F50.

DATA AVAILABILITY

PIC simulations were performed on Pleiades at the NASA Advanced Supercomputing Division, and the simulation data are available upon request from the authors.

REFERENCES

- 1A. Retinò, D. Sundkvist, A. Vaivads, F. Mozer, M. André, and C. J. Owen, "In situ evidence of magnetic reconnection in turbulent plasma," *Nat. Phys.* **3**, 235 (2007).
- 2D. Sundkvist, A. Retinò, A. Vaivads, and S. D. Bale, "Dissipation in turbulent plasma due to reconnection in thin current sheets," *Phys. Rev. Lett.* **99**, 025004 (2007).
- 3T. D. Phan, G. Paschmann, C. Twitty, F. S. Mozer, J. T. Gosling, J. P. Eastwood, M. Øieroset, H. Rème, and E. A. Lucek, "Evidence for magnetic reconnection initiated in the magnetosheath," *Geophys. Res. Lett.* **34**, L14104, <https://doi.org/10.1029/2007GL030343> (2007).
- 4E. Yordanova, Z. Vörös, A. Varsani, D. B. Graham, C. Norgren, Y. V. Khotyaintsev, A. Vaivads, E. Eriksson, R. Nakamura, P.-A. Lindqvist, G. Marklund, R. E. Ergun, W. Magnes, W. Baumjohann, D. Fischer, F. Plaschke, Y. Narita, C. T. Russell, R. J. Strangeway, O. L. Contel, C. Pollock, R. B. Torbert, B. J. Giles, J. L. Burch, L. A. Avanov, J. C. Dorelli, D. J. Gershman, W. R. Paterson, B. Lavraud, and Y. Saito, "Electron scale structures and magnetic reconnection signatures in the turbulent magnetosheath," *Geophys. Res. Lett.* **43**, 5969, <https://doi.org/10.1002/2016GL069191> (2016).
- 5Z. Vörös, E. Yordanova, A. Varsani, K. J. Genestreti, Y. V. Khotyaintsev, W. Li, D. B. Graham, C. Norgren, R. Nakamura, Y. Narita, F. Plaschke, W. Magnes, W. Baumjohann, D. Fischer, A. Vaivads, E. Eriksson, P.-A. Lindqvist, G. Marklund, R. E. Ergun, M. Leitner, M. P. Leubner, R. J. Strangeway, O. L. Contel, C. Pollock, B. J. Giles, R. B. Torbert, J. L. Burch, L. A. Avanov, J. C. Dorelli, D. J. Gershman, W. R. Paterson, B. Lavraud, and Y. Saito, "MMS observation of magnetic reconnection in the turbulent magnetosheath," *J. Geophys. Res.* **112**, 11442 (2017).
- 6A. Chasapis, W. H. Matthaeus, T. N. Parashar, O. LeContel, A. Retinò, H. Breuillard, Y. Khotyaintsev, A. Vaivads, B. Lavraud, E. Eriksson, T. E. Moore, J. L. Burch, R. B. Torbert, P.-A. Lindqvist, R. E. Ergun, G. Marklund, K. A. Goodrich, F. D. Wilder, M. Chutter, J. Needell, D. Rau, I. Dors, C. T. Russell, G. Le, W. Magnes, R. J. Strangeway, K. R. Bromund, H. K. Leinweber, F. Plaschke, D. Fischer, B. J. Anderson, C. J. Pollock, B. L. Giles, W. R. Paterson, J. Dorelli, D. J. Gershman, L. Avanov, and Y. Saito, "Electron heating at kinetic scales in magnetosheath turbulence," *Astrophys. J.* **836**, 247 (2017).
- 7T. D. Phan, J. P. Eastwood, M. A. Shay, J. F. Drake, B. U. Ö. Sonnerup, M. Fujimoto, P. A. Cassak, M. Øieroset, J. L. Burch, R. B. Torbert, A. C. Rager, J. C. Dorelli, D. J. Gershman, C. Pollock, P. S. Pyakurel, C. C. Haggerty, Y. Khotyaintsev, B. Lavraud, Y. Saito, M. Oka, R. E. Ergun, A. Retino, O. L. Contel, M. R. Argall, B. L. Giles, T. E. Moore, F. D. Wilder, R. J. Strangeway, C. T. Russell, P. A. Lindqvist, and W. Magnes, "Electron magnetic reconnection without ion coupling in Earth's turbulent magnetosheath," *Nature* **557**, 202 (2018).
- 8F. D. Wilder, R. E. Ergun, J. L. Burch, N. Ahmadi, S. Eriksson, T. D. Phan, K. A. Goodrich, J. Shuster, A. C. Rager, R. B. Torbert, B. L. Giles, R. J. Strangeway, F. Plaschke, W. Magnes, P. A. Lindqvist, and Y. V. Khotyaintsev, "The role of the parallel electric field in electron-scale dissipation at reconnecting currents in the magnetosheath," *J. Geophys. Res.* **123**, 6533, <https://doi.org/10.1029/2018JA025529> (2018).
- 9S. Wang, L.-J. Chen, N. Bessho, M. Hesse, L. B. Wilson III, B. Giles, T. E. Moore, C. T. Russell, R. B. Torbert, and J. L. Burch, "Observational evidence of magnetic reconnection in the terrestrial bow shock transition region," *Geophys. Res. Lett.* **46**, 562, <https://doi.org/10.1029/2018GL080944> (2019).
- 10I. Gingell, S. J. Schwartz, J. P. Eastwood, J. L. Burch, R. E. Ergun, S. Fuselier, D. J. Gershman, B. L. Giles, Y. V. Khotyaintsev, B. Lavraud, P.-A. Lindqvist, W. R. Paterson, T. D. Phan, C. T. Russell, J. E. Stawarz, R. J. Strangeway, R. B. Torbert, and F. Wilder, "Observations of magnetic reconnection in the transition region of quasi-parallel shocks," *Geophys. Res. Lett.* **46**, 1177 (2019).
- 11Z. Z. Chen, H. S. Fu, Z. Wang, C. M. Liu, and Y. Xu, "Evidence of magnetic nulls in the reconnection at bow shock," *Geophys. Res. Lett.* **46**, 10209, <https://doi.org/10.1029/2019GL084360> (2019).

- ¹²I. Gingell, S. J. Schwartz, J. P. Eastwood, J. E. Stawarz, J. L. Burch, R. E. Ergun, S. A. Fuselier, D. J. Gershman, B. L. Giles, Y. V. Khotyaintsev, B. Lavraud, P.-A. Lindqvist, W. R. Paterson, T. D. Phan, C. T. Russell, R. J. Strangeway, R. B. Torbert, and F. Wilder, "Statistics of reconnecting current sheets in the transition region of Earth's bow shock," *J. Geophys. Res.* **125**, e2019JA027119 (2020).
- ¹³H. Karimabadi, V. Roytershteyn, H. X. Vu, Y. A. Omelchenko, J. Scudder, W. Daughton, A. Dimmock, K. Nykyri, M. Wan, D. Sibeck, M. Tatineni, A. Majumdar, B. Loring, and B. Geveci, "The link between shocks, turbulence, and magnetic reconnection in collisionless plasmas," *Phys. Plasmas* **21**, 062308 (2014).
- ¹⁴I. Gingell, S. J. Schwartz, D. Burgess, A. Johlander, C. T. Russell, J. L. Burch, R. E. Ergun, S. Fuselier, D. J. Gershman, B. L. Giles, K. A. Goodrich, Y. V. Khotyaintsev, B. Lavraud, P.-A. Lindqvist, R. J. Strangeway, K. Trattner, R. B. Torbert, H. Wei, and F. Wilder, "MMS observations and hybrid simulations of surface ripples at a marginally quasi-parallel shock," *J. Geophys. Res. Space Phys.* **122**, 11003, <https://doi.org/10.1002/2017JA024538> (2017).
- ¹⁵Y. Matsumoto, T. Amano, T. N. Kato, and M. Hoshino, "Stochastic electron acceleration during spontaneous turbulent reconnection in a strong shock wave," *Science* **347**, 974 (2015).
- ¹⁶A. Bohdan, J. Niemiec, O. Kobzar, and M. Pohl, "Electron pre-acceleration at non-relativistic high-Mach-number perpendicular shocks," *Astrophys. J.* **847**, 71 (2017).
- ¹⁷N. Bessho, L.-J. Chen, S. Wang, M. Hesse, and L. B. Wilson III, "Magnetic reconnection in a quasi-parallel shock: Two-dimensional local particle-in-cell simulation," *Geophys. Res. Lett.* **46**, 9352, <https://doi.org/10.1029/2019GL083397> (2019).
- ¹⁸S. P. Gary, "Electromagnetic ion/ion instabilities and their consequences in space plasmas: A review," *Space Sci. Rev.* **56**, 373 (1991).
- ¹⁹P. Hellinger and A. Mangeney, "Electromagnetic ion beam instabilities: Oblique pulsations," *J. Geophys. Res.* **104**, 4669, <https://doi.org/10.1029/1998JA001157> (1999).
- ²⁰J. R. Kan and D. W. Swift, "Structure of the quasi-parallel bow shock: Results of numerical simulations," *J. Geophys. Res.* **88**, 6919, <https://doi.org/10.1029/JA088iA09p06919> (1983).
- ²¹D. Winske and K. B. Quest, "Electromagnetic ion beam instabilities: Comparison of one- and two-dimensional simulations," *J. Geophys. Res.* **91**, 8789, <https://doi.org/10.1029/JA091iA08p08789> (1986).
- ²²K. B. Quest, "Theory and simulation of collisionless parallel shocks," *J. Geophys. Res.* **93**, 9649, <https://doi.org/10.1029/JA093iA09p09649> (1988).
- ²³J. R. Kan, M. E. Mandt, and L. H. Lyu, "Quasi-parallel collisionless shocks," *Space Sci. Rev.* **57**, 201 (1991).
- ²⁴M. Scholer, "Upstream waves, shocklets, short large-amplitude magnetic structures and the cyclic behavior of oblique quasi-parallel collisionless shocks," *J. Geophys. Res.* **98**, 47, <https://doi.org/10.1029/92JA01875> (1993).
- ²⁵M. Scholer, M. Fujimoto, and H. Kucharek, "Two-dimensional simulations of supercritical quasi-parallel shocks: Upstream waves, downstream waves, and shock re-formation," *J. Geophys. Res.* **98**, 18971, <https://doi.org/10.1029/93JA01647> (1993).
- ²⁶D. Krauss-Varban, "Waves associated with quasi-parallel shocks: Generation, mode conversion and implications," *Adv. Space Res.* **15**, 271 (1995).
- ²⁷K. Tsubouchi and B. Lembège, "Full particle simulations of short large-amplitude magnetic structures (SLAMS) in quasi-parallel shocks," *J. Geophys. Res.* **109**, A02114, <https://doi.org/10.1029/2003JA010014> (2004).
- ²⁸M. S. Weidl, D. Winske, and C. Niemann, "Three regimes and four modes for the resonant saturation of parallel ion-beam instabilities," *Astrophys. J.* **873**, 57 (2019).
- ²⁹L. B. Wilson III, "Low frequency waves at and upstream of collisionless shocks," in *Low-Frequency Waves in Space Plasmas*, Geophysical Monograph Series, edited by A. Keiling, D.-H. Lee, and V. Nakariakov (American Geophysical Union, Washington, DC, 2016), Vol. 216, pp. 269–291.
- ³⁰P. V. Heuer, M. S. Weidl, R. S. Dorst, D. B. Schaeffer, S. K. P. Tripathi, S. Vincena, C. G. Constantin, C. Niemann, L. B. Wilson III, and D. Winske, "Laboratory observations of ultra-low-frequency analog waves driven by the right-hand resonant ion beam instability," *Astrophys. J.* **891**, L11 (2020).
- ³¹S. J. Schwartz, D. Burgess, W. P. Wilkinson, R. L. Kessel, M. Dunlop, and H. Lühr, "Observations of short large-amplitude magnetic structures at a quasi-parallel shock," *J. Geophys. Res.* **97**, 4209, <https://doi.org/10.1029/91JA02581> (1992).
- ³²M. Scholer, H. Kucharek, and I. Shinohara, "Short large-amplitude magnetic structures and whistler wave precursors in a full-particle quasi-parallel shock simulation," *J. Geophys. Res.* **108**, 1273, <https://doi.org/10.1029/2002JA009820> (2003).
- ³³T. Umeda, Y. Omura, and H. Matsumoto, "An improved masking method for absorbing boundaries in electromagnetic particle simulations," *Comput. Phys. Commun.* **137**, 286 (2001).
- ³⁴M. E. Mandt, R. E. Denton, and J. F. Drake, "Transition to whistler mediated magnetic reconnection," *Geophys. Res. Lett.* **21**, 73, <https://doi.org/10.1029/93GL03382> (1994).
- ³⁵P. Sharma Pyakurel, M. A. Shay, T. D. Phan, W. H. Matthaeus, J. F. Drake, J. M. TenBarge, C. C. Haggerty, K. G. Klein, P. A. Cassak, T. N. Parashar, M. Swisdak, and A. Chasapis, "Transition from ion-coupled to electron-only reconnection: Basic physics and implications for plasma turbulence," *Phys. Plasmas* **26**, 082307 (2019).
- ³⁶A. Mallet, "The onset of electron-only reconnection," *J. Plasma Phys.* **86**, 905860301 (2020).
- ³⁷P. A. Cassak and M. A. Shay, "Scaling of asymmetric magnetic reconnection: General theory and collisional simulations," *Phys. Plasmas* **14**(10), 102114 (2007).
- ³⁸X. Blanco-Cano, G. Le, and C. T. Russell, "Identification of foreshock waves with 3-s periods," *J. Geophys. Res.* **104**, 4643, <https://doi.org/10.1029/1998JA001103> (1999).
- ³⁹J. P. Eastwood, A. Balogh, E. A. Lucek, C. Mazelle, and I. Dandouras, "On the existence of Alfvén waves in the terrestrial foreshock," *Ann. Geophys.* **21**, 1457 (2003).
- ⁴⁰Y. Hobara, S. N. Walker, M. Balikhin, O. A. Pokhotelov, M. Dunlop, H. Nilsson, and H. Rème, "Characteristics of terrestrial foreshock ULF waves: Cluster observations," *J. Geophys. Res.* **112**, A07202, <https://doi.org/10.1029/2006JA012142> (2007).
- ⁴¹H. K. Wong and C. W. Smith, "Electron beam excitation of upstream waves in the whistler mode frequency range," *J. Geophys. Res.* **99**, 13373, <https://doi.org/10.1029/94JA00821> (1994).
- ⁴²K. Sauer and R. D. Sydora, "Beam-excited whistler waves at oblique propagation with relation to STEREO radiation belt observations," *Ann. Geophys.* **28**, 1317 (2010).
- ⁴³S. Matsukiyo and M. Scholer, "On microinstabilities in the foot of high Mach number perpendicular shocks," *J. Geophys. Res.* **111**, A06104, <https://doi.org/10.1029/2005JA011409> (2006).
- ⁴⁴A. J. Hull, L. Muschietti, O. Le Contel, J. C. Dorelli, and P.-A. Lindqvist, "MMS observations of intense whistler waves within Earth's supercritical bow shock: Source mechanism and impact on shock structure and plasma transport," *J. Geophys. Res.* **125**, e2019JA027290 (2020).
- ⁴⁵T. Umeda, Y. Kidani, S. Matsukiyo, and R. Yamazaki, "Modified two-stream instability at perpendicular collisionless shocks: Full particle simulations," *J. Geophys. Res.* **117**, A03206, <https://doi.org/10.1029/2011JA017182> (2012).
- ⁴⁶T. Umeda, Y. Kidani, S. Matsukiyo, and R. Yamazaki, "Microinstabilities at perpendicular collisionless shocks: A comparison of full particle simulations with different ion to electron mass ratio," *Phys. Plasmas* **19**, 042109 (2012).
- ⁴⁷H. S. Fu, A. Vaivads, Y. V. Khotyaintsev, V. Olshevsky, M. André, J. B. Cao, S. Y. Huang, A. Retinò, and G. Lapenta, "How to find magnetic nulls and reconstruct field topology with MMS data?," *J. Geophys. Res.* **120**, 3758, <https://doi.org/10.1002/2015JA021082> (2015).
- ⁴⁸R. B. Torbert, I. Dors, M. R. Argall, K. J. Genestreti, J. L. Burch, C. J. Farrugia, T. G. Forbes, B. L. Giles, and R. J. Strangeway, "A new method of 3-D magnetic field reconstruction," *Geophys. Res. Lett.* **47**, e2019GL085542, <https://doi.org/10.1029/2019GL085542> (2020).
- ⁴⁹R. E. Denton, R. B. Torbert, H. Hasegawa, I. Dors, K. J. Genestreti, M. R. Argall, D. Gershman, O. L. Contel, J. L. Burch, C. T. Russell, R. J. Strangeway, B. L. Giles, and D. Fischer, "Polynomial reconstruction of the reconnection magnetic field observed by multiple spacecraft," *J. Geophys. Res.* **125**, e2019JA027481 (2020).